International Journal of Microwave and Wireless Technologies

cambridge.org/mrf

Design, developments, and applications of 5G antennas: a review

Mohit Pant and Leeladhar Malviya

Shri G. S. Institute of Technology and Science, Indore, India

Review Paper

Cite this article: Pant M, Malviya L (2023). Design, developments, and applications of 5G antennas: a review. *International Journal of Microwave and Wireless Technologies* **15**, 156–182. https://doi.org/10.1017/S1759078722000095

Received: 18 November 2021
Revised: 8 January 2022
Accepted: 10 January 2022
First published online: 9 February 2022

Keywords:
Fifth-generation (5G); antenna array; multiple-input multiple-output (MIMO); mutual coupling; mm-wave; gain; isolation; diversity; beamforming

Author for correspondence:
Mohit Pant, E-mail: ermohitpant@gmail.com

Abstract

As the demand for high data rates is increasing day by day, fifth-generation (5G) becomes the leading-edge technology in wireless communications. The main objectives of the 5G communication system are to enhance the data rates (up to 20 Gbps) and capacity, ultra-low latency (1 ms), high reliability, great flexibility, and enhance device to device communication. The mentioned objectives lead to the hunting of the millimeter-wave frequency range which lies from 30 to 300 GHz for 5G wireless communications. To design such high capacity, low latency, and flexible systems, antenna design is one of the crucial parts. In this paper, a survey is presented on various antenna designs with their fabrication on different types of substrates such as Rogers RT/duroid 5880, Rogers RO4003C, Taconic TLY-5, etc., at different 5G frequency bands. The different configurations of antennas that covered antenna arrays, multiple-input multiple-output (MIMO) antennas, phased antennas, and beamforming antennas are discussed in detail with their applications. The design of MIMO antennas in the 5G frequency band occupied less space so mutual coupling reduction techniques are required for maintaining the required gain, efficiency, and isolation. This paper is also focused on the mutual coupling reduction techniques and diversity in MIMO antennas.

Introduction

The rapid and dynamic increase of mobile data growth and the use of smart phones, tablets, and Wi-Fi hotspot devices are generating remarkable challenges for wireless service providers to win a battle against a global bandwidth scarcity. Today's cellular providers are committed to providing best quality, high-resolution, low latency, ultra-reliable videos and multimedia applications for wireless devices [1–3]. Fifth generation (5G) of cellular communication systems have been deployed in the world with each new mobile generation emerging in every decade since 1980. The first generation (1G) of analog FM cellular systems came in 1980, second-generation (2G) of digital technology in 1992, third generation (3G) in 2001, fourth-generation (4G), long-term evolution (LTE) in 2011, and 5G in 2020 [4]. The evolution from 1G to 5G based on design, implementation, carrier frequency, data rate, spectral efficiency, latency, services, multiplexing techniques, core network, and name of the corresponding technologies are summarized in Table 1.

The 5G played an important role to provide seamless connectivity for the present wireless communication systems and overcomes the limitations of the previous wireless systems. Third generation partnership project (3GPP) defines three main 5G scenarios: enhanced mobile broadband (eMBB) at 10 Gbps, ultra-reliable and low latency communications (uRLLC) at 1 ms, and massive machine type communications (mMTC) at 1 million per km [5, 6]. In addition to ultra-low latency, highly reliable systems and to boost digital connectivity, 5G is in great demand. As correlated with the present 4G, 5G wireless communications are significantly different in various performance parameters such as gigabit per second (Gbps) data rate, end-to-end latency of <1 ms, exceptionally less energy consumption, and ultra-dense traffic volume. The band lies from 0.45 to 6.0 GHz specified as FR1 (frequency range 1) band, and from 24.25 to 52.6 GHz referred to as FR2 (frequency range 2) band. Due to the drastic increase in the mobile data demand, the spectrum available in the sub-6 GHz band is insufficient to fulfill the user's demands, so researchers and telecommunication companies are looking forward to a higher frequency spectrum from 6 to 300 GHz which will be employed for future wireless generations [7, 8].

ITU has declared the following spectrum for the deployment of 5G communications which consists of 3.4–3.6, 5–6, 24.25–27.5, 37–43.5, 45.5–50.2, 50.4–52.6, 66–76, and 81–86 GHz. Also, the Federal Communications Commission (FCC) has taken a major initiative to provide 5G additional spectrum in the following categories: high band: 24 GHz, 28 GHz, 37 GHz, 39 GHz, and 47 GHz, mid-band: 2.5 GHz, 3.5 GHz, and 3.7–4.2 GHz, low band: 600 MHz, 800 MHz, and 900 MHz, unlicensed: 6 GHz and above 95 GHz band. The mid-5G new radio (NR) bands such as n78 (3.3–3.8 GHz), n77 (3.3–4.2 GHz), n79 (4.4–5.0 GHz), n40 (2.3–2.4 GHz), n41 (2.496–2.690 GHz), n38 (2.57–2.62 GHz) are the active 5G NR networks in

Table 1. Comparison of different generations of wireless technologies

Generation	1G	2G	2.5G	3G	4G	5G
Design year	1970	1980	1985	1990	2000	2010
Implementation	1980	1991	1991	2001	2001	2020
Carrierfrequency (GHz)	0.00003	1.8	2.2	1.8–2.5	2–8	3–300
Data rate	1.9 kbps	14.4 kbps	384 kbps	2 Mbps	200 Mbps	>1 Gbps
Spectralefficiency (bps/Hz)	0.0015	0.17	0.172	0.24–0.51	15	30
Services	Analog voice	Digital voice	Higher capacity packetized data	Higher capacity broadband	Internet protocol (IP) based	eMBB mMTC
Multiplexing	Frequency division multiple access (FDMA)	Code division multiple access (CDMA), time division multiple access (TDMA)	TDMA, CDMA	CDMA	Orthogonal frequency division multiple access, single carrier-FDMA	Orthogonal frequency division multiplexing, beam division multiple access
Core network	Public switched telephone network (PSTN)	PSTN	PSTN, packet network	Packet network	IP backbone	Flatter internet protocol, 5G-Network interfacing
Technologies	Advance mobile phone system, Nordic mobile telephony, total access communication system	Global system for mobile communication (GSM), CDMA	General packet radio service, enhanced data rates for GSM evolution	Wideband-CDMA, CDMA-2000	Long-term evolution, world-wideinteroperability for microwave access	MIMO, mm-waves
References	[1, 2]	[3, 4]	[5, 6]	[7–10]	[9–12]	[10–15]

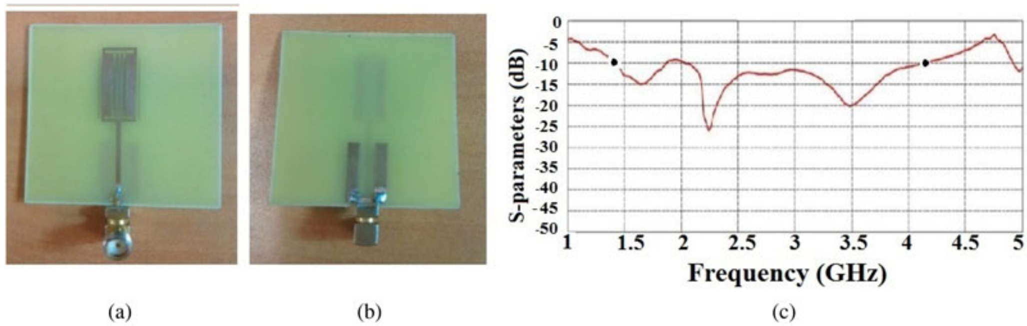

Fig. 1. Slotted 5G antenna: fabricated (a) front view, (b) back view, and (c) *S*-parameters. [36].

the 2–8 GHz frequency band. These bands have employed time-division duplexing, which is considered as a spectrum-efficient scheme and has the capability to enclose a wide geographical area for 5G communication systems for better coverage. TDD bands n78, n40, and n41 have become the industry concern to achieve higher data rates [9–11].

The FR1 bands are envisaged to carry much of the traditional cellular mobile communication traffic. At the millimeter-wave (mm-wave) or FR2 band which lies in 24.25–52.6 GHz band, the signal-to-noise ratio (SNR) and signal-to-interference ratio (SIR) deteriorate because the electromagnetic waves suffer from the free space path loss and blockage. In the sub-6 GHz spectrum, the main attraction is on the 3.5 GHz band which has 400 MHz bandwidth (3.4–3.8 GHz), and is commercially available in many parts of the world, and can be used with the existing communication system hardware with minor changes [12–15].

5G antenna designs in sub-6 GHz (2–8 GHz)

In this section, various designs of 5G antennas, antenna arrays, multiple-input multiple-output (MIMO) antennas and MIMO antenna arrays, beamforming antennas in the frequency range 2–8 GHz are discussed along with their designs and results.

2–8 GHz: single-element antennas

An important component of any wireless communication system is the antenna. A microstrip patch antenna is a pioneer in wireless communication devices. The development of microstrip patch antennas has offered many prospects in the present and future antenna designs, fabrication, and implementation [16, 17]. The main advantages of microstrip patch antennas are its low cost, light weight, low profile, and easy fabrication [18]. Microstrip patch antennas come with different shapes such as rectangular, triangular, square, hexagonal, circular, annular ring, and elliptical [19–22]. In mm-wave frequency, size of the antenna, substrate property, and thickness are the important considerations. The microstrip antennas are designed and fabricated on dielectric substrates such as FR-4, Rogers RT/duroid 5880/5870, Taconic TLY-5, Taconic TLY-5, Megtron 6, Astra MT77, and Rogers RO4003C [23, 24].

The conventional microstrip antennas have some limitations such as single-operating frequency, low impedance bandwidth, low gain, larger size, and polarization problems. There are a number of techniques that have been reported for enhancing the parameters of conventional microstrip antennas such as stacking, different feeding techniques, frequency selective surfaces (FSS), electromagnetic band gap (EBG), photonic band gap (PBG), and metamaterials [25, 26]. Microstrip patch antennas are widely used in 5G sub-6 GHz and mm-wave systems. They are a strong choice for 5G base station antenna designs. However, its narrow bandwidth has confined its application to 5G base station antennas. Many techniques and solutions have been proposed by researchers to improve the bandwidth of patch antennas [27–29]. A sub-6 GHz band will be able to cover the larger geographical areas for 5G coverage, but will not be able to provide high downlink speed [30], while an mm-wave 5G technology will be able to provide high downlink speeds, but at the cost of less geographical area coverage. The frequency band 4.8–5.0 GHz of sub-6 GHz is allocated as an official band for 5G wireless systems [31]. In the sub-6 GHz spectrum, the focus will be on the 3.5 GHz band having a 400 MHz bandwidth (3.4–3.8 GHz), as is commercially available globally.

The concept of metamaterials in the antennas at sub-6 GHz and mm-wave frequency has provided the improvement in antenna parameters such as gain and bandwidth. A metamaterial can be defined as an artificial homogeneous electromagnetic structure, designed for interaction and control of electromagnetic waves, and it contains unique properties which are not readily found in nature. For metamaterials, the structure size should be less than a quarter wavelength. Metamaterials can be classified based on their electromagnetic properties such as double negative (DNG) materials, left-handed (LH) materials, right-handed (RH) materials, negative refractive index (NRI) materials, magneto materials, and artificial magnetic conductors (AMCs). Metamaterials can also be termed as EBG, PBG, and defected ground structure (DGS) [32–35].

A compact sub-6 GHz antenna was designed by employing an FR-4 substrate ($\epsilon_r = 4.4$, thickness $(h) = 1$ mm, loss tangent $(\tan\delta) = 0.025$) with a size of $20 \times 12\,\text{mm}^2$. The desired frequency and wide bandwidth of 1.4–4.2 GHz were obtained which covered the 3.1–4.2 GHz 5G operating frequency band by employing three vertical slots, two horizontal slots in the patch, and the U-shaped ground structure in the ground plane. The antenna achieved a gain of 2.3 dBi. The fabricated views (front and back) and *S*-parameters are shown in Figs 1(a), 1(b), and 1(c) [36].

A multiband stack antenna which covered LTE and sub-6 GHz bands was designed by employing multilayers of FR-4 substrates each having ($\epsilon_r = 4.4$, $h = 1.6$ mm, $\tan\delta = 0.025$) a size of $180 \times 60\,\text{mm}^2$ in the dual operating band 0.66–0.79 and 3.28–3.78 GHz. In the design, the lower substrate consists of an elliptical patch which supports generation of 700 MHz band (LTE-R), and the upper substrate consists of five different circular

https://doi.org/10.1017/S1759078722000095 Published online by Cambridge University Press

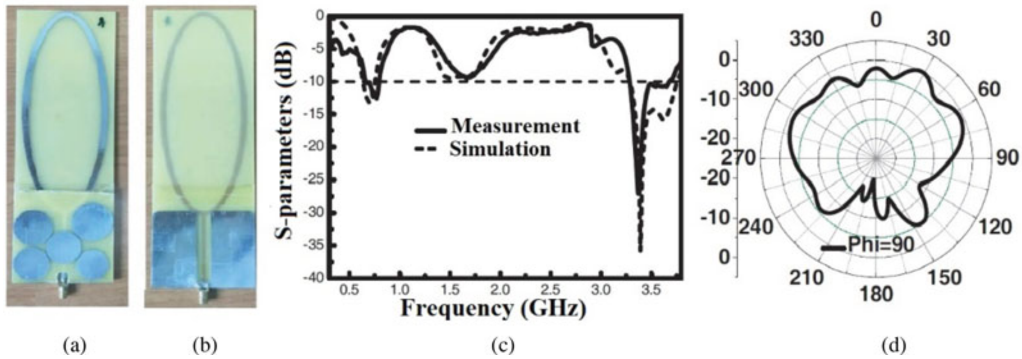

Fig. 2. Dual band 5G antenna: fabricated (a) front view, (b) back view, (c) *S*-parameters, and (d) radiation pattern. [37].

patches which were made for resonating the antenna at 3.5 GHz (5G lower band) frequency and also contributed to enhance the bandwidth. The gain in the bands were 2.4 dBi at 0.7 GHz and 6.1 dBi at 3.5 GHz, respectively. The fabricated views (front and back) are shown in Figs 2(a) and 2(b). The *S*-parameters and radiation pattern are illustrated in Figs 2(c) and 2(d) [37].

To get a wide operating band and to cover n77/n78/n79 sub-6 GHz 5G bands, an antenna was designed on an FR-4 substrate ($\epsilon_r = 4.4$, $h = 1.5$ mm, $\tan\delta = 0.025$) with a size of 30×20 mm^2 and operated in the 3.15–5.55 GHz frequency band. The slotted patch and the partial ground were employed. The antenna achieved a gain of 1.87–2.69 dBi and radiation efficiency of 68.7–79.6% in the whole band. The fabricated views (front and back) are shown in Figs 3(a) and 3(b), *S*-parameters and radiation patterns are shown in Figs 3(c) and 3(d) [38].

To achieve a stable radiation pattern, a low cost and low profile antenna was designed on two layers of an FR-4 substrate ($\epsilon_r = 4.4$, $h_1 = 1.5$ mm, $h_2 = 0.4$ mm, $\tan\delta = 0.025$) with a size of 63×51.2 mm^2 which operated in the 2.8–5.2 GHz frequency band for 5G mobile communication systems. The top layer had three vertical dielectric pieces with two folded walls which were also designed in the upper layer of the substrate to support the patch. The three elliptical slots were employed for proper impedance matching. The antenna achieved a gain of 6.2 dBi and average radiation efficiency of 64% in the whole band. The fabricated front view is shown in Fig. 4 (a), *S*-parameters and radiation patterns are shown in Figs 4 (b) and 4(c) [39].

A patch antenna with DNG metamaterial was designed by employing a complementary split ring resonator (CSRR) on FR-4 dielectric substrate ($\epsilon_r = 4.4$, $h = 1.62$ mm, $\tan\delta = 0.025$) with a size of 48×35 mm^2 for the n78 operating band in 3.3–3.8 GHz. The 6×6 CSRR was able to increase the gain and control the radiation pattern to minimize the specific absorption rate (SAR). The antenna achieved a gain of 5.5 dBi and radiation efficiency of 87% in the complete operating frequency band. The fabricated views (front and back) are shown in Figs 5(a) and 5(b). The *S*-parameters are shown in Fig. 5(c) [40].

A low profile rectangular slot dual-band antenna was designed and fabricated on an FR-4 substrate ($\epsilon_r = 4.4$, $h = 0.8$ mm, $\tan\delta = 0.025$) with a size of 36×31 mm^2 for operating in the lower 5G frequency bands such as n77 (3.3–4.2 GHz), n78 (3.3–3.8 GHz), and n79 (4.4–5 GHz). For creating a dual-band, the antenna was loaded with an inverted U-shaped stub in terms of ground arm and folded T-shaped feedline at the ground plane. The peak gain was 7.17 dBi with 80% radiation efficiency in the whole band. The fabricated views (front and back) are shown in Figs 6(a) and 6(b), and *S*-parameters and radiation patterns are shown in Figs 6 (c) and 6(d) [41].

2–8 GHz: antenna arrays

There are many antennas having low gain, low directivity, and omnidirectional radiation patterns. Therefore, array antennas are required to provide high gain to single port antennas. In this case, multiple patches/elements are connected to the single port.

A 2×2 graphene antenna array was designed on an FR-4 substrate ($\epsilon_r = 4.4$, $h = 1.6$ mm, $\tan\delta = 0.025$) with a size of 60×70 mm^2 for the 3.4–3.6 GHz frequency band, which covered sub-6 GHz 5G frequency band. A low loss T-type power divider was employed to excite the antenna array. The antenna array achieved a gain of 6.77 dBi with 99.99% radiation efficiency at 3.51 GHz resonant frequency. The fabricated front view is shown in Fig. 7(a), *S*-parameters and radiation patterns are shown in Figs 7(b) and 7(c). From the results, it was found that with the reflection coefficient, gain, and radiation pattern, the graphene antenna exhibited an equivalent performance as compared to a copper antenna [42].

A 1×8 circular fractal antenna array was designed on an FR-4 substrate ($\epsilon_r = 4.4$, $h = 1.6$ mm, and $\tan\delta = 0.025$) with a size of 100×300 mm^2 which resonated at multiple frequencies. For obtaining fractal geometry, first, a circular slot of radius 3.3 mm was cut down from the center of each circular patch, then four more slots were cut again from each circular slot having a radius of 1.1 mm. The maximum gain achieved was 9.22 dBi with a radiation efficiency of 80.56% at 3.80 GHz resonant frequency. The fabricated front view and *S*-parameters are shown in Figs 8(a) and 8(b) [43].

To convert linear polarization into right-hand circular polarization, a diagonal rectangular slot was etched at the middle of the antenna elements on a Taconic RF-35 substrate ($\epsilon_r = 3.5$, $h = 3.04$ mm, and $\tan\delta = 0.0018$). The sequential-phase feeding network consists of three T-power dividers which circulate the input power to the outputs with equal magnitude and orthogonal in phase. The four parasitic elements were used to enhance bandwidth and gain. The 2×2 antenna array of dimensions 110×110 mm^2 achieved a gain of 11.4–15.8 dBi in the operating band of 4.6–6.1 GHz. The fabricated (front and back) views are shown in Figs 9 (a) and 9(b). The *S*-parameters are shown in Fig. 9(c) [44].

2–8 GHz: MIMO antennas and MIMO antenna arrays

Wireless systems that employed antenna elements/arrays at both the transmitter and receiver are known as MIMO. It is one of

https://doi.org/10.1017/S1759078722000095 Published online by Cambridge University Press

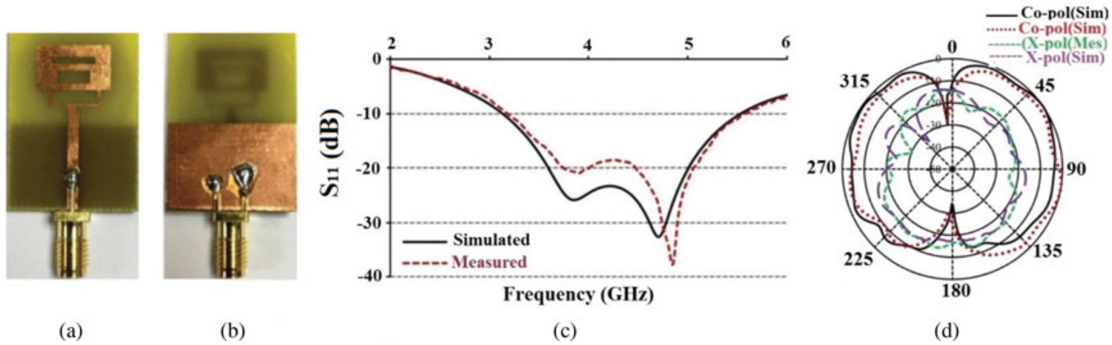

Fig. 3. Dual band 5G antenna: fabricated (a) front view, (b) back view, (c) *S*-parameters, and (d) radiation patterns. [38].

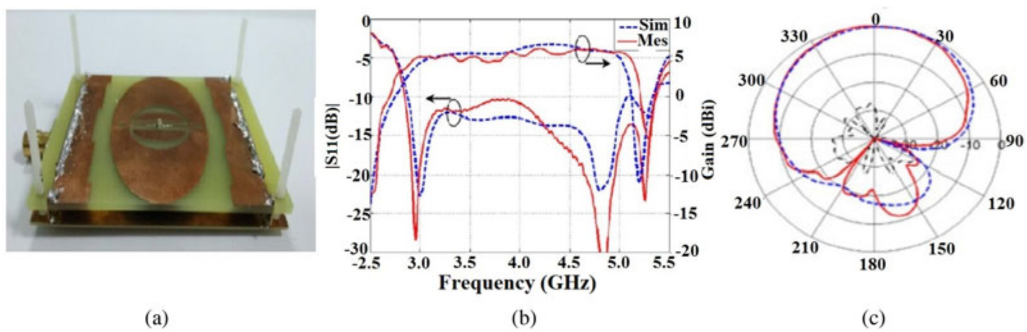

Fig. 4. Wide band 5G antenna: fabricated (a) front view, (b) *S*-parameters, and (c) radiation patterns. [39].

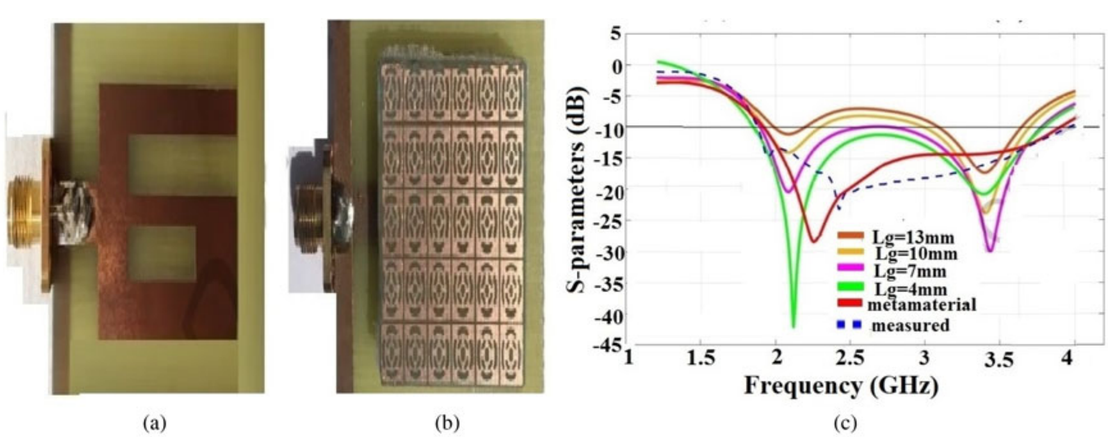

Fig. 5. Metamaterial-based antenna: fabricated (a) front view, (b) back view, and (c) *S*-parameters. [40].

the prime technologies that is used in both 4G and 5G wireless communication systems to overcome the disadvantages of single input single output (SISO). It works efficiently in non-line of sight (NLOS) wireless communication. The main advantages of MIMO antennas are to boost the spectral efficiency, enhanced channel capacity, premium services within limited power in dense scattering environments. The capacity of SISO and MIMO can be obtained using equations (1) and (2), respectively [45–47]:

$$C = B\log_2(1 + SNR) \tag{1}$$

$$C = \log_2\left[\det\left(I_{N_r} + \frac{\rho}{NN_t}HH^*\right)\right] \tag{2}$$

where N_t and N_r are the transmit and receiver antenna elements, I_{N_r} is the $N_r \times N_r$ identity matrix, ρ is the mean SNR per receiver branch, and superscript $*$ denotes the Hermitian transpose, H is the channel matrix, and H^* is the transpose of channel matrix.

In spite of many advantages, the design and fabrication of MIMO antenna in confined space is a big challenge in the 5G antennas. The crucial requirement of MIMO antenna is that the radiating elements should be as small as possible, well-matched,

https://doi.org/10.1017/S1759078722000095 Published online by Cambridge University Press

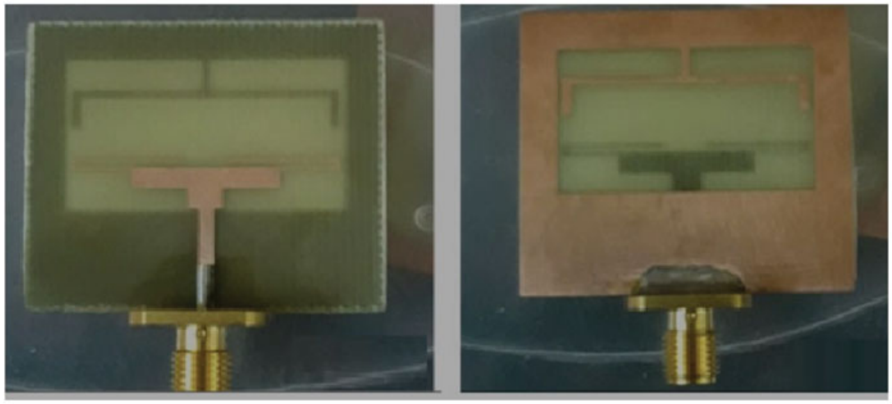

(a) (b)

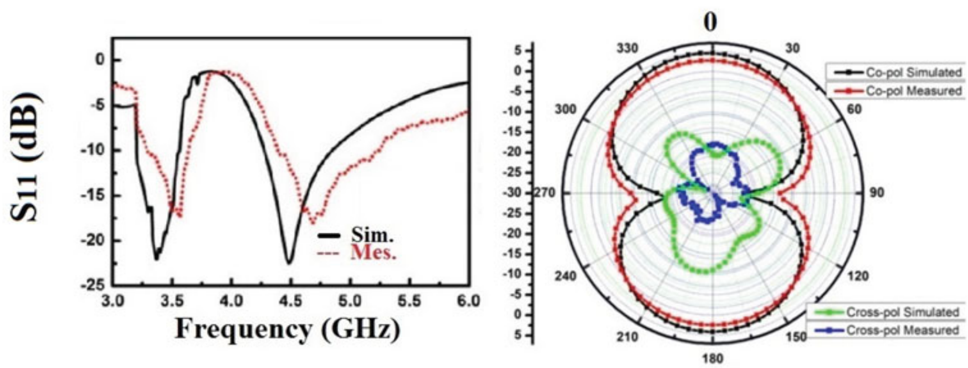

(c) (d)

Fig. 6. Dual band rectangular slot antenna: fabricated (a) front view, (b) back view, (c) *S*-parameters, and (d) radiation patterns. [41].

and should have low mutual coupling with nearby elements. Mutual coupling is induced among the radiating elements of the antennas because of the compactness and portability compulsion of the 5G wireless devices [48, 49]. Mutual coupling can be defined as the energy absorbed by a closeby antenna when one antenna is radiating. The mutual coupling leads to change the input impedance, reflection coefficients, and radiation characteristics of the MIMO antennas. Mutual coupling can be defined by equations (3) and (4), respectively [50, 51]:

$$MC_{ij} = \exp\left(-\frac{2d_{ij}(\alpha + j\pi)}{\lambda}\right),\ i \neq j \tag{3}$$

$$MC_{ij} = 1 - \frac{1}{N}\sum_{i}\sum_{i\neq j} M_{ij} \tag{4}$$

where MC_{ij} and d_{ij} are the mutual coupling and distance between the ith and jth antenna elements, respectively, N is the number of array elements, and α is the parameter that dominates the coupling level [52].

The close proximity of radiating elements results in mutual coupling or correlation, which reduces the isolation and achievable performance [53]. The performance of the MIMO system can be characterized by the parameters such as efficiency, radiation patterns, operating bandwidths, envelope correlation coefficient (ECC), mean effective gain (MEG), total active reflection coefficient (TARC), diversity gain (DG), and channel capacity [54]. The scattering parameters S_{12} or S_{21} between the ports are not sufficient to include the effect of all *S*-parameters, therefore correlation coefficient is necessary to be calculated in MIMO antennas. It is a measure to describe how the two antennas are isolated from each other.

ECC is the square of the correlation coefficient. There are two ways to calculate the correlation coefficient, one is by employing *S*-parameters as given in equation (5) and second one is determined by using far-field radiation patterns of the MIMO antennas as given in equation (6) [55]:

$$ECC = \frac{\left|\sum_{n=1}^{N} S_{i,n}^{*} S_{n,j}^{*}\right|}{\sqrt{\left|\prod_{k=(i,j)}\left[1 - \sum_{n=1}^{N} S_{i,n}^{*} S_{n,k}^{*}\right]\right|}} \tag{5}$$

$$ECC = |\rho_e|^2 = \frac{\left|\iint\left[\overrightarrow{F_1}(\theta,\phi) \times \overrightarrow{F_2}(\theta,\phi)\right]d\Omega^2\right|}{\iint|\overrightarrow{F_1}(\theta,\phi)|^2 d\Omega \iint|\overrightarrow{F_2}(\theta,\phi)|^2 d\Omega} \tag{6}$$

where ρ_e is the correlation coefficient, $F_1(\theta,\ \phi)$ and $F_2(\theta,\ \phi)$ are the field radiation patterns of the antennas when any port is excited and other port is properly terminated to match the load and vice versa, and Ω is the solid angle.

https://doi.org/10.1017/S1759078722000095 Published online by Cambridge University Press

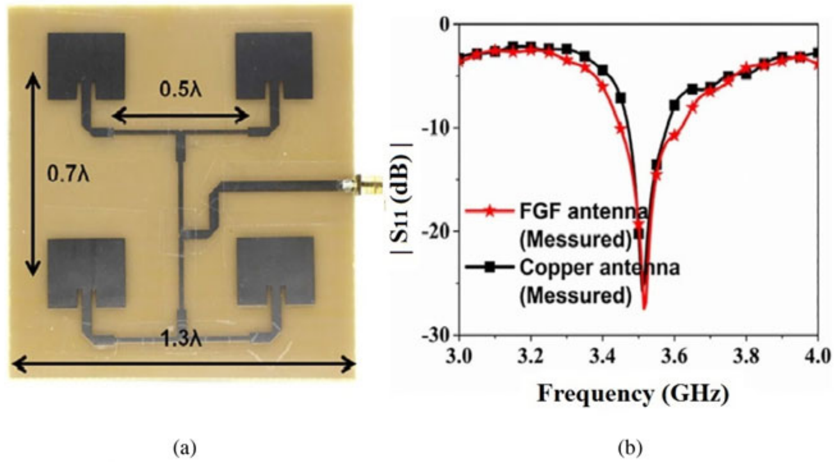

Fig. 7. Graphene-based 5G antenna array: fabricated (a) front view, (b) *S*-parameters, and (c) radiation patterns. [42].

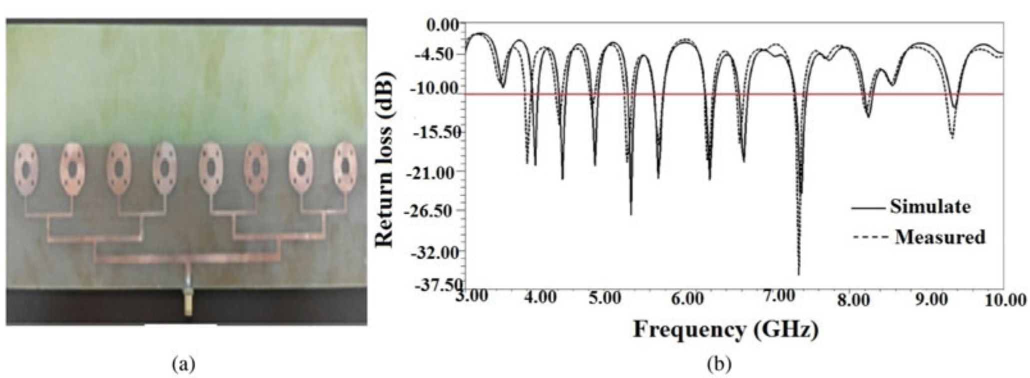

Fig. 8. 1 × 8 circular fractal antenna array: fabricated (a) front view and (b) *S*-parameters. [43].

The ECC may be described by equation (7) [56]:

$$\rho_e = 1 - \frac{\eta_{max}^2}{\eta_i \eta_j} \tag{7}$$

where η_i and η_j are the total efficiencies of the antennas i and j, and η_{max} is the multiplexing efficiency.

Similarly, the antenna DG is used to check the effectiveness of the diversity. For satisfactory operation of MIMO antennas, DG should be closed to 10 dB. It can be determined by calculating ECC, using equation (8) [57]:

$$DG = 10\sqrt{1 - |ECC|^2} \tag{8}$$

MEG is one of the significant specifications for defining the performance of the antenna in real propagation or fading environments. It is the unique parameter that determines the effect of the antenna on the link budget. In general, MEG can be

https://doi.org/10.1017/S1759078722000095 Published online by Cambridge University Press

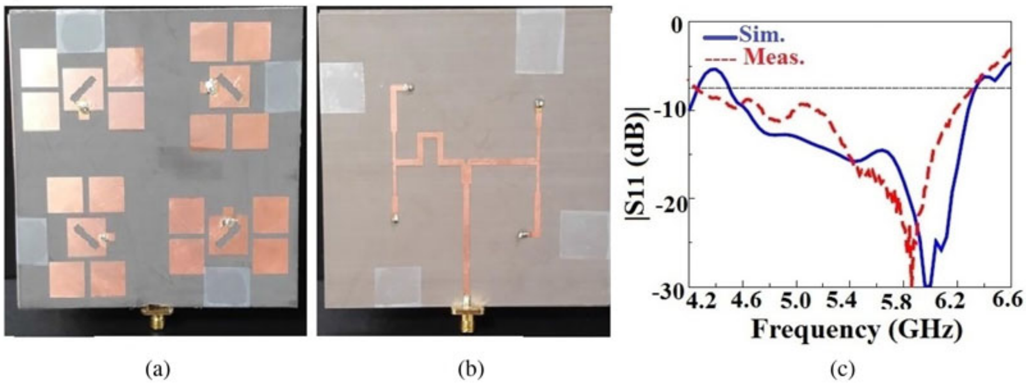

Fig. 9. Circularly polarized antenna array: fabricated (a) front view, (b) back view, and (c) *S*-parameters. [44].

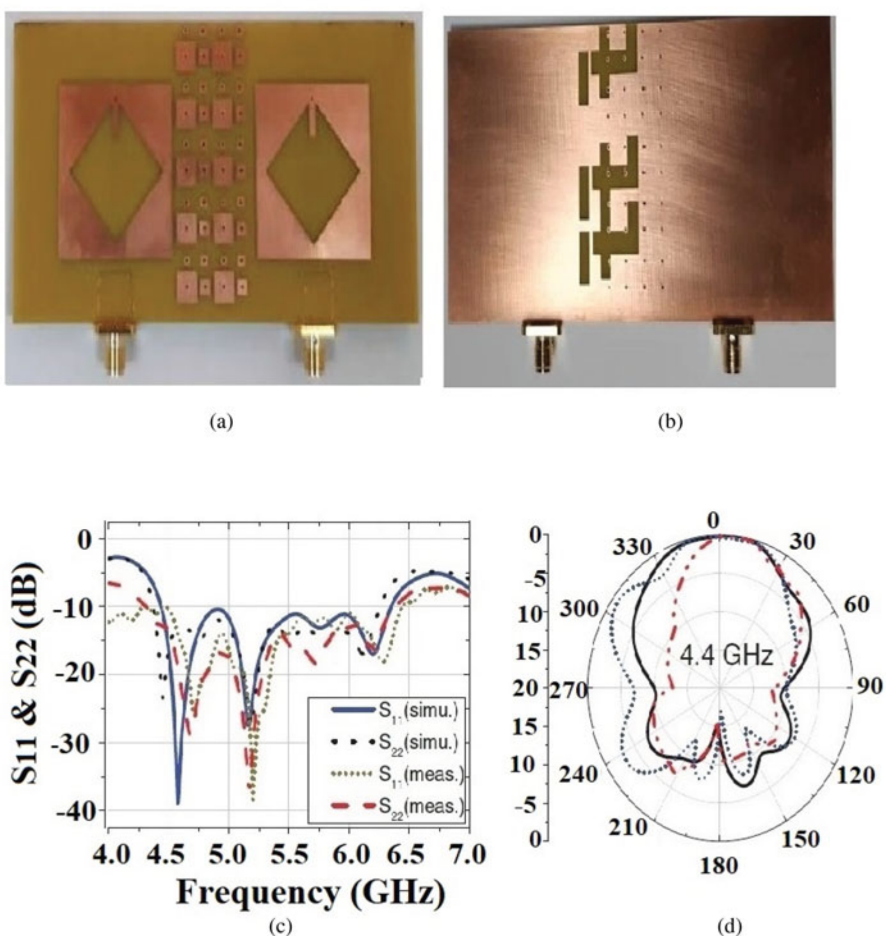

Fig. 10. 5G MIMO antenna array with DGS: fabricated (a) front view, (b) back view, (c) *S*-parameters, and (d) radiation patterns. [71].

defined as the sum of gains of the NLOS and LOS components. It can be used to determine the average signal strength of each antenna and is given by equation (9) [58–60]:

$$MEG_i = 0.5\left(1 - \sum_{j=1}^{k} S_{i,j}\right) \tag{9}$$

where i and j represent the antenna under testing and number of antennas, respectively.

The MEG can be expressed by equations (10) and (11), respectively [61, 62]:

$$MEG_j = \oint\Big(\tfrac{XPR}{1+XPR}P_{\theta j}(\Omega)G_{\theta j}(\Omega) + \tfrac{1}{1+XPR}P_{\theta j}(\Omega)G_{\theta j}(\Omega)\Big) \tag{10}$$

https://doi.org/10.1017/S1759078722000095 Published online by Cambridge University Press

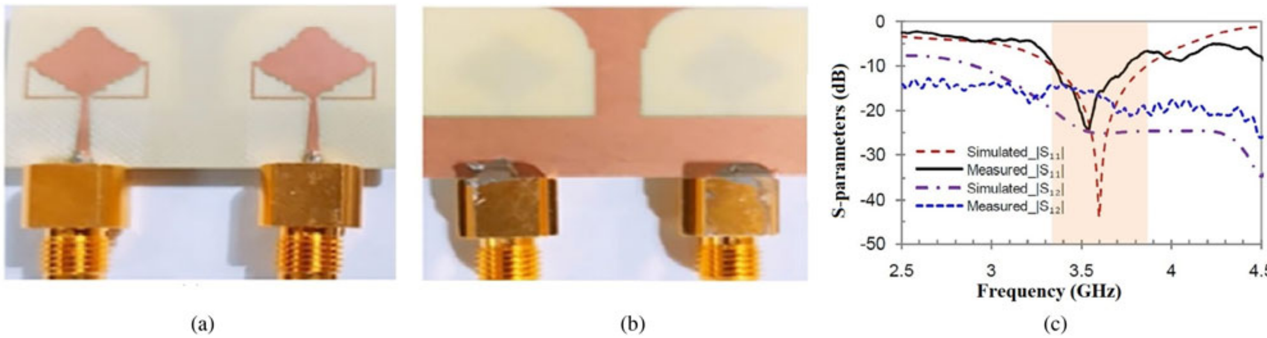

Fig. 11. 5G MIMO antenna array with grounded stub: fabricated (a) front view, (b) back view with T-shaped stub, and (c) *S*-parameters. [72].

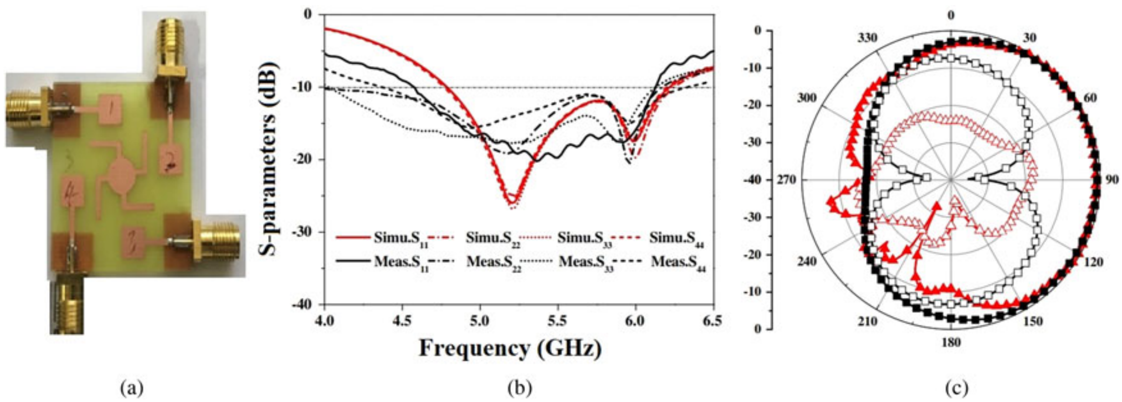

Fig. 12. Pattern diversity MIMO antenna: fabricated (a) front view, (b) *S*-parameters, (c) and radiation patterns. [73].

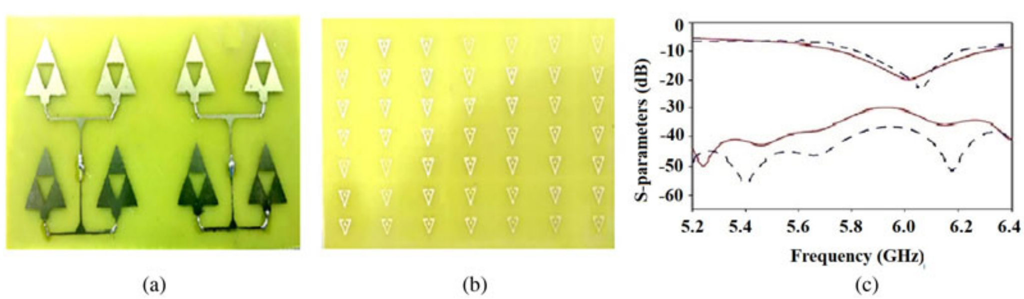

Fig. 13. 4 × 2 MIMO antenna array: fabricated (a) front view, (b) back view, and (c) *S*-parameters. [74].

$$MEG_j = \int_0^{2\pi}\left[\frac{XPR}{1+XPR}G_{\theta j}\left(\frac{\pi}{2},\phi\right) + \frac{1}{1+XPR}G_{\phi j}\left(\frac{\pi}{2},\phi\right)\right] \tag{11}$$

where XPR is the cross-polarization ratio and P_θ, P_ϕ denote the weighted angular spectrum or weighted probability function of the angle of arrival of the stochastic components in the θ and ϕ polarizations, respectively.

Here, θ and ϕ are the elevation and azimuth angles in a spherical coordinate system. Similarly, a scattering matrix is not sufficient for the proper definition of the efficiency and bandwidth of the MIMO antenna system, therefore TARC is more appropriate for characterization of the MIMO antenna system. For an N-port lossless antenna having $[S]$ as scattering matrix, TARC is defined as the square root of the ratio of the sum of the power available at all the ports subtracted by the radiated power to the total available power and is given by equation (12):

$$\Gamma_a^t = \sqrt{\frac{available\ power - radiated\ power}{available\ power}} \tag{12}$$

For N-elements, TARC is defined by equation (13):

$$\Gamma_a^t = \sqrt{\frac{\sum_{i=1}^{N}|b_i|^2}{\sum_{i=1}^{N}|a_i|^2}} \tag{13}$$

https://doi.org/10.1017/S1759078722000095 Published online by Cambridge University Press

Table 2. Comparison of single-element antennas, antenna arrays, MIMO antennas, and MIMO antenna arrays for 2–8 GHz frequency band

Ref. no.	Freq. band/bands (GHz)	No. of ports	No. of elements	Dimensions (mm^3)	Gain (dBi)	Efficiency (%)	Isolation (dB)	Applications
[36]	3.1–4.2	01	01	20 × 12 × 0.8	2.3	–	–	5G Mobile devices.
[37]	3.28–3.78	01	01	180 × 60 × 1.6	6.1	–	–	5G mobile network.
[38]	3.15–5.55	01	01	30 × 20 × 1.5	2.69	79.6	–	5G wireless communications.
[39]	2.8–5.2	01	01	63 × 51.2 × 1.5	6.2	64.0	–	5G wireless networks.
[40]	3.3–3.8	01	01	48 × 35 × 1.62	5.5	87.0	–	4G-5G communications
[41]	3.2–3.6, 4.3–5.2	01	01	31 × 36 × 1.8	7.17	80.0	–	Future generation 5G communications.
[42]	3.4–3.6	01	04	70 × 60 × 0.025	6.77	99.99	–	5G mobile communications.
[43]	3.5–3.8, 3.8-4.4, 4.8–5.4	01	08	100 × 300 × 1.6	9.22	80.56	–	Multiband wireless applications.
[44]	4.6–6.1	01	04	110 × 110 × 3.04	11.4–15.8	–	–	Wideband wireless communications.
[71]	4.4–6.4	02	05	57.5 × 120.8 × 1.6	5.6	62.0	10–50	5G wideband wireless applications.
[72]	3.3–3.8	02	02	20 × 35 × 0.8	2.2	–	≥10	Future sub-6 GHz applications.
[73]	3.3–3.6, 4.8–5.0	04	04	30 × 30 × 0.8	4.02	70-80	15.4	WLAN/5G/WiFi applications.
[74]	5.2–6.4	02	08	38 × 107 × 1.6	14.05	96.2	30	Wireless communications.

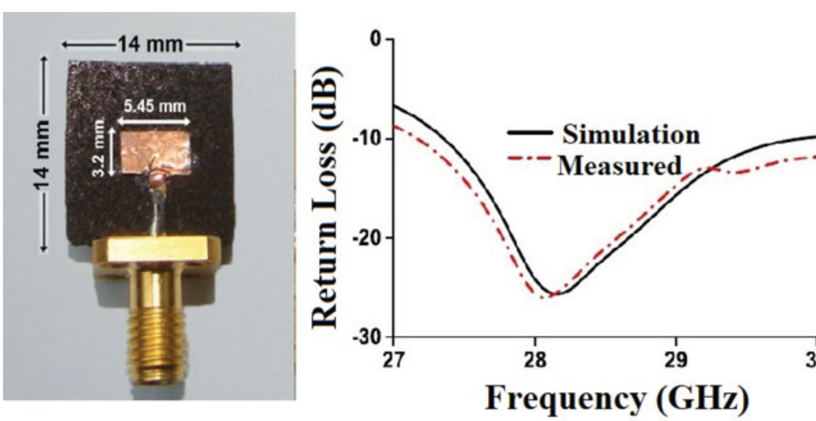

(a) (b)

Fig. 14. 5G single patch antenna: fabricated (a) front view and (b) *S*-parameters. [87].

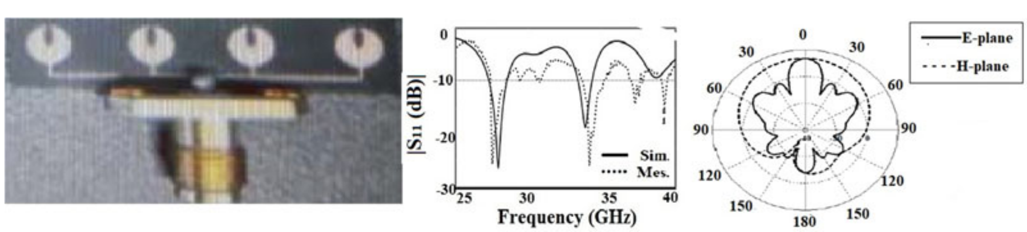

(a) (b) (c)

Fig. 15. 1 × 4 5G elliptical antenna array: fabricated (a) front view, (b) *S*-parameters, and (c) radiation patterns. [88].

where a_i and b_i are the incident and reflected signals, respectively, in a multiport network. Γ_a^t is a real-valued variable that lies between 0 and 1.

TARC is very useful and is an MIMO performance metric, as it considers the impact of random phases of incoming signals at each antenna element. For the *N*-port set of MIMO antennas, if

https://doi.org/10.1017/S1759078722000095 Published online by Cambridge University Press

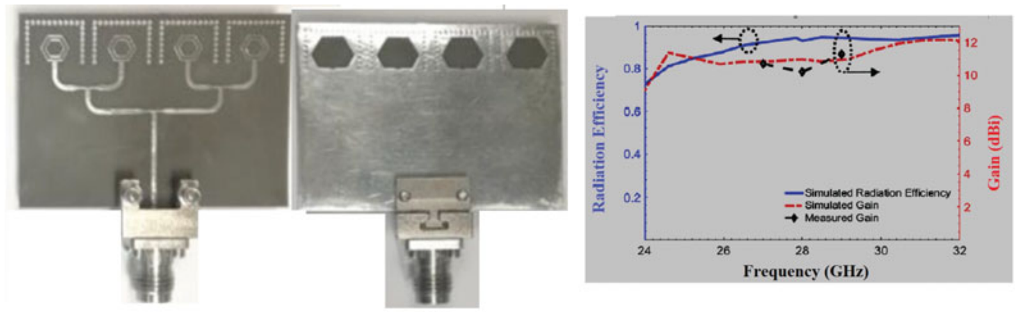

(a) (b) (c)

Fig. 16. 1 × 4 broadband 5G antenna array: fabricated (a) front view, (b) back view, and (c) gain–efficiency plot. [93].

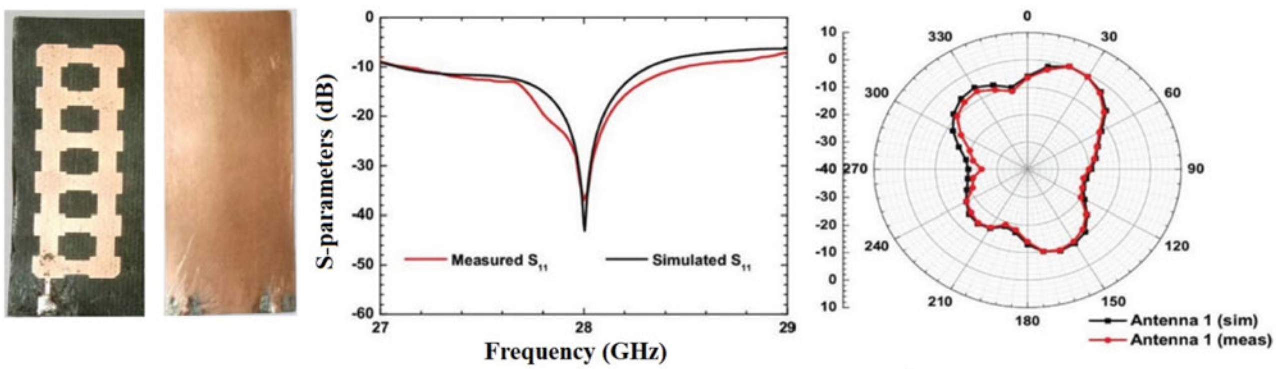

(a) (b) (c) (d)

Fig. 17. High gain antenna array: fabricated (a) front view, (b) back view, (c) *S*-parameters, and (d) radiation patterns. [94].

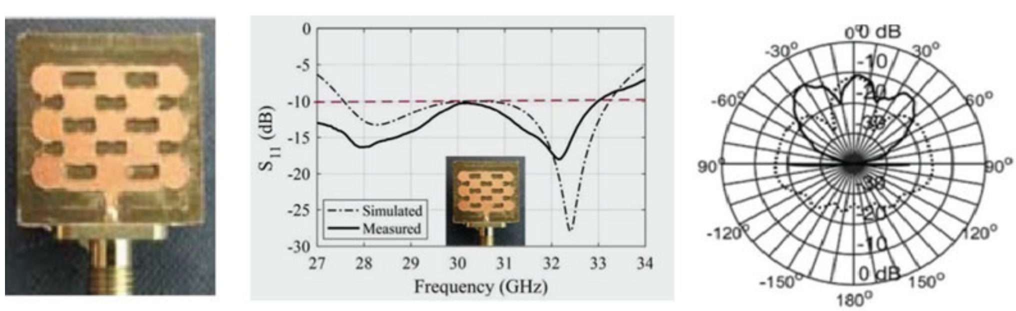

(a) (b) (c)

Fig. 18. 5G grid antenna array: fabricated (a) front view, (b) *S*-parameters, and (c) radiation patterns. [95].

θ is an independent and identically distributed Gaussian phase of a random process and reference phase θ_0 is neglected, then TARC can be defined by equation (14) [63, 64]:

$$TARC = N^{-1/2}\sqrt{\sum_{i=1}^{n}\left|\sum_{k=1}^{n} S_{ik}e^{j\theta_{k-1}}\right|^2} \tag{14}$$

For $N = 2$, above expression can be written as equation (15):

$$TARC = \frac{\sqrt{|S_{12}e^{j\theta_0} + S_{11}e^{j\theta_1}|^2 + |S_{21}e^{j\theta_0} + S_{22}e^{j\theta_1}|^2}}{\sqrt{2}} \tag{15}$$

Many techniques have been explored by researchers to minimize the mutual coupling and enhance the isolation among the radiating elements. For example, DGS, EBG, FSS, neutralization lines, parasitic elements, metamaterial based structures, isolators

https://doi.org/10.1017/S1759078722000095 Published online by Cambridge University Press

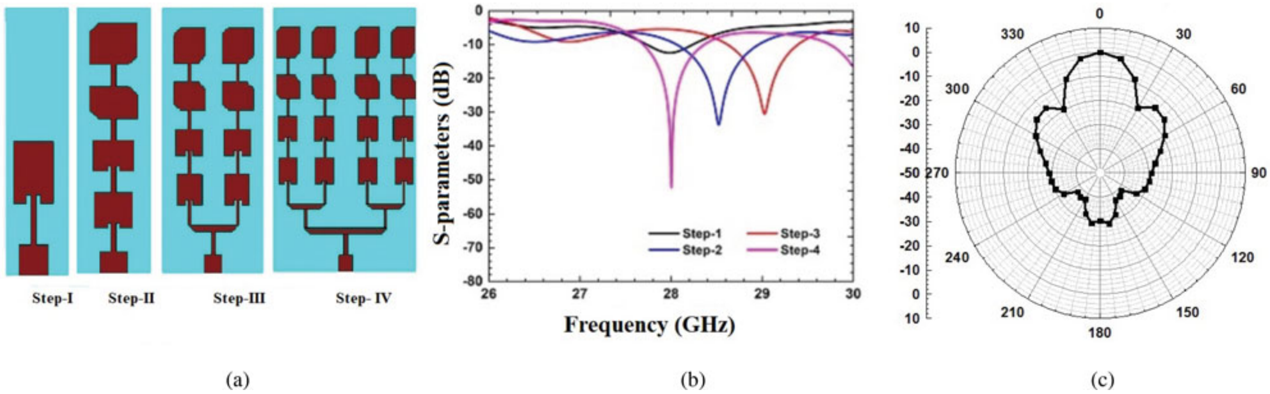

Fig. 19. 16 elements antenna array: (a) design steps, (b) *S*-parameters, and (c) radiation patterns. [96].

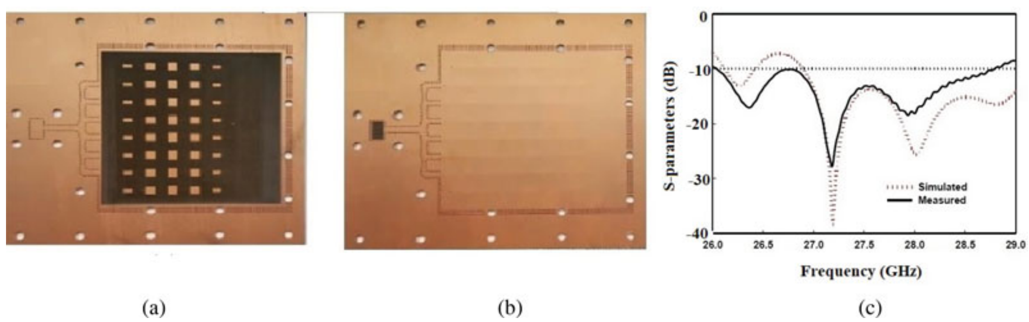

Fig. 20. 6 × 5 proximity coupled antenna: fabricated (a) front view, (a) back view, and (c) *S*-parameters. [97].

such as T-shaped, circular, SRR, and CSRR, etc. are used to lower the effect of mutual coupling [65–70].

The three double "F"-shaped defect was employed in DGS to enhance the isolation bandwidth of microstrip-slotted patch antenna designed on two layers of FR-4 substrate ($\epsilon_r = 4.4$, $h = 1.6$ mm, $\tan\delta = 0.025$) of dimensions 57.5×110 mm^2 having 0.09 mm distance between them. A 2 × 5 asymmetrical arrays of EBG patches were also used to further minimize the isolation from 10 to 50 dB over the entire frequency band lies from 4.4 to 6.4 GHz. The antenna achieved a gain of 5.6 dBi with a radiation efficiency of 62% in the operating frequency band. The fabricated (front and back) views are shown in Figs 10(a) and 10(b), *S*-parameters and radiation patterns are shown in Figs 10(c) and 10(d) [71].

Similarly, for improving isolation and better impedance matching, an MIMO antenna array was designed on FR-4 epoxy substrate ($\epsilon_r = 4.4$, $h = 0.8$ mm, $\tan\delta = 0.025$) with a size of 20×35 mm^2 for 5G n78 band (3.3–3.8 GHz) with an altered T-shaped stub was placed between the two tapered rhombus-shaped radiators excited through tapered feeding with DGS. The antenna achieved a gain of 2.34 dBi with a radiation efficiency of 93% in the 3.34–3.87 GHz operating frequency band. An additional stub was also connected through the center of the radiator to obtain the required resonant frequency of 3.6 GHz. The isolation reported was >20 dB and 530 MHz bandwidth with ECC < 0.02 and *TARC* < 0.5. The antenna achieved gain of 2.34 dBi at 3.6 GHz resonant frequency. The fabricated (front and back) views are shown in Figs 11(a) and 11(b). The *S*-parameters are exemplified in Fig. 11(c) [72].

A 4×4 MIMO antenna array with pattern diversity was designed on an FR-4 substrate ($\epsilon_r = 4.4$, $h = 0.8$ mm, and $\tan\delta = 0.025$) with a size of 30×30 mm^2 for 5G n78 (3.3–3.6 GHz) and n79 (4.8–5 GHz) frequency bands. A parasitic patch acts as a decoupling structure consisting of a circular patch and four L-shaped arms employed on the top of the substrate were placed orthogonally. The design showed isolation >15 dB and the gain was 4.02 dBi at 5.95 GHz. The radiation efficiency was varied from 67 to 82% in the entire 4.58–6.12 GHz frequency band. The fabricated front view is illustrated in Fig. 12(a), the *S*-parameters and radiation patterns are delineated in Figs 12(b) and 12(c) [73].

A 4 × 2 MIMO antenna array placed on the top of 7 × 7 metamaterial superstrate with a spacing of 5 mm between them was designed on an FR-4 substrate ($\epsilon_r = 4.4$, $h = 1.6$ mm, $\tan\delta = 0.025$) with a size of 107×58 mm^2. The advantages of DNG unit cell superstrate has as compared to MIMO antenna array without DNG superstrate are the bandwidth increased from 210 MHz (5.65–6.4 GHz) to 750 MHz (5.91–6.12 GHz), boost the gain from 11.1 to 14.05 dBi, and enhanced the isolation from 30 to 38 dB. The radiating efficiency was 96.2% at 5.6 GHz resonant frequency. The fabricated (front and back) views are shown in Figs 13 (a) and 13(b). The *S*-parameters are shown in Fig. 13 (c) [74].

The comparison of the sub-6 GHz antenna, antenna arrays, and MIMO antennas are given in Table 2.

5G antenna designs in 24–40 GHz frequency bands

In this section, various designs of 5G antennas, antennas arrays, MIMO antennas, MIMO antenna arrays, and beamforming

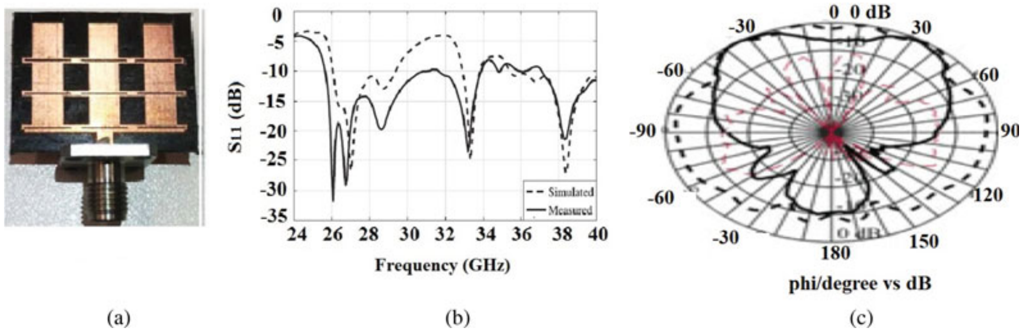

Fig. 21. 3 × 3 Franklin antenna array: fabricated (a) front view, (b) *S*-parameters, and (c) radiation patterns. [98].

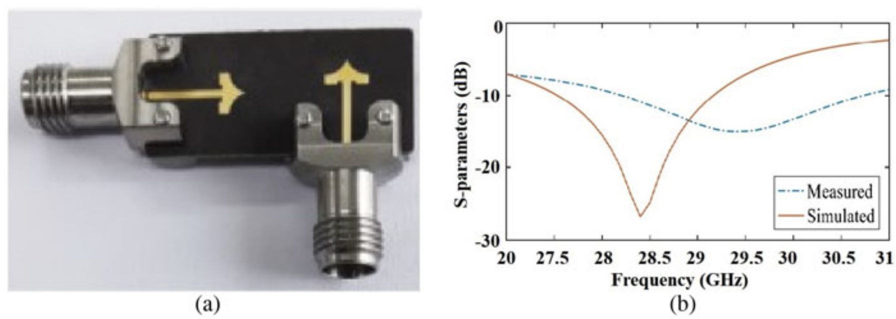

Fig. 22. Two-element MIMO-antenna: fabricated (a) front view and (b) *S*-parameters. [101].

antennas from frequency range 24 to 40 GHz are discussed along with their designs and results.

24–40 GHz: single-element antenna and antenna arrays

In this section, the 5G antenna designs with 24–40 GHz frequency range are covered with all the details. As the spectrum lying in the sub-6 GHz is becoming congested due to the increasing demand for high data rates, the necessity of mm-wave bands such as 28, 38, 60, and 73 GHz for 5G communication systems is vital. In China 24.25–27.5 and 37–42.5 GHz and in the USA 27.5–28.5 and 37–39 GHz bands have been determinant as prominent frequency bands for 5G wireless communication systems. The high-frequency bands are able to give a fast speed and high capacity, depending on the distance between the users and the cell site [75–77].

The telecommunication companies such as NTT DOCOMO, CMCC, KT, Verizon, T-mobiles, and AT&T are planning to utilize the 24.25–29.5 and 37–40 GHz 5G frequency spectrum and companies such as Orange, Telecom Italia, and British Telecom are going to support 31.8–33.4 GHz frequency band. Millimeter spectrum provides higher bandwidth and capacity. However, as the frequency increases the mm-wave suffers from propagation loss, blockage, and interference. In addition, mm-wave frequency bands suffer from atmospheric losses for example as the size of raindrops is comparable to mm-wave wavelength so scattering loss has occurred. The total attenuation caused by atmospheric gases and rain is given by equation (16) [78, 79]:

$$\gamma = \gamma_G + \gamma_R = \gamma_0 + \gamma_w + kR^\alpha \qquad (16)$$

where γ_G is the sum of the attenuations due to oxygen and water vapor, respectively, γ_R is attenuation (dB/km) due to rainfall, R is the rain rate (mm/h), k and α are coefficients which depend on frequency f (GHz).

At 28 GHz the path loss in dense urban NLOS environment is given by equation (17), for $d < 100$ and equation (18) for $d > 100$, respectively:

$$PL(d) = 96.9 + 15.1\log_{10}(d) \qquad (17)$$

$$PL(d) = 127 + 87\log_{10}(d/100) \qquad (18)$$

where d is the distance in m.

At 28 GHz the path loss is significantly higher as compared to the sub-6 GHz band, according to the free space path loss given by equation (19) an additional 22.9 dB of losses can take place from 2 to 28 GHz frequency range. To mitigate such losses antenna array size of higher gains, MIMO antenna, massive MIMO antennas, and beamforming techniques are highly needed and desirable:

$$L_p = 92.4 + 20\log(f) + 20\log(d) \qquad (19)$$

The sum of electric fields from two-element arrays separated by distance d is given by equation (20):

$$E(r) = E_1(r)e^{j\psi/2} + E_2(r)e^{-j\psi/2} \qquad (20)$$

where E_1 and E_2 are the electric fields by first and second elements and ψ is the phase difference which is define by equation (21) [80, 81]:

$$\psi = kd\cos(\theta) \qquad (21)$$

where $k = 2\pi/\lambda$.

https://doi.org/10.1017/S1759078722000095 Published online by Cambridge University Press

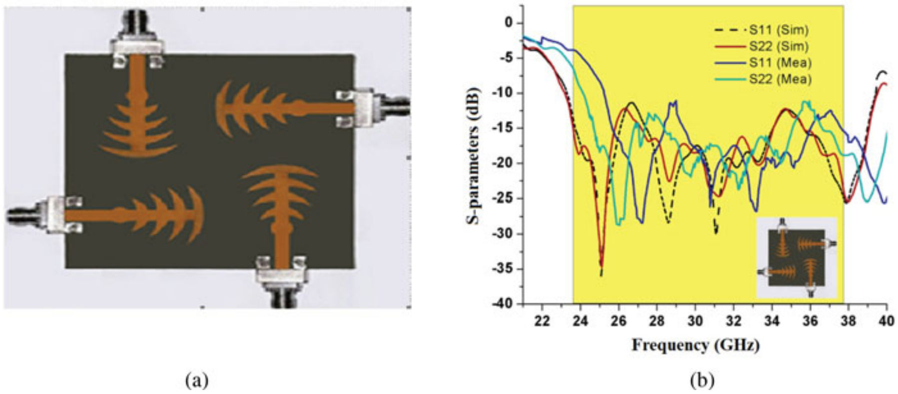

Fig. 23. Four-elements MIMO antenna: fabricated (a) front view and (b) *S*-parameters. [102].

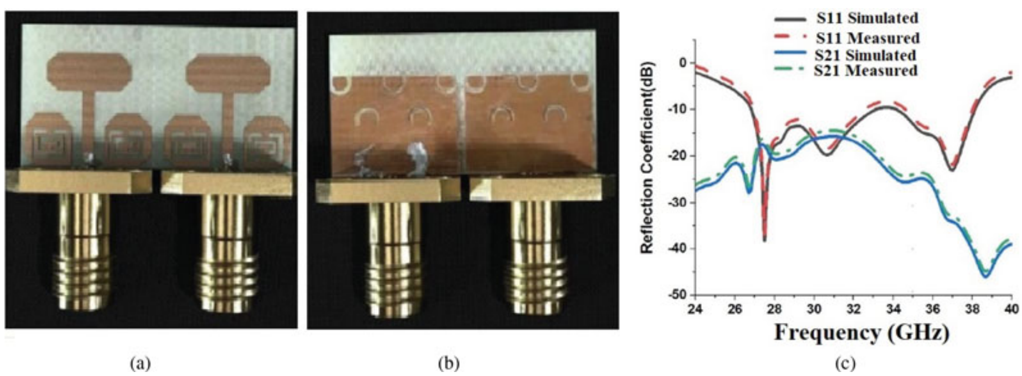

Fig. 24. 5G MIMO antenna with T-stub fabricated: (a) front view, (b) back view, and (c) *S*-parameters. [103].

The radiation pattern of an antenna array can be obtained by the product of the radiation pattern of a single element multiplied by an array factor (AF) which is given by equation (22):

$$AF = 2\cos\left(\frac{kd\cos\theta}{2}\right) \tag{22}$$

Consider α be the progressive shift between the N radiating elements then the AF is obtained by equation (23):

$$AF = \sum_{m=0}^{N-1} e^{jkmd\cos\theta + jm\alpha} \tag{23}$$

For the circular array the AF can be calculated by equation 24 [82, 83]:

$$AF = \sum_{n=0}^{N-1} e^{jka(r_1+r_2)} \tag{24}$$

where $r_1 = \cos(2\pi n/N)\sin\theta\cos\phi$ and $r_2 = \sin(2\pi n/N)\sin\theta\sin\phi$.

There are many antennas and antenna arrays designed for 5G applications for 28–40 GHz operating frequency band using different feeding techniques such as inset feed, series feed, corporate feed, and corporate-series feed [84–86]. A 28 GHz patch antenna was designed on a manganese zinc ferrite substrate ($\epsilon_r = 7$, $h = 1.00$ mm, $\tan\delta = 0.003$) with a size of $14 \times 14\,\text{mm}^2$. The -10 dB impedance bandwidth was 27.23–29.89 GHz and the gain achieved was 5.44 dBi with a radiation efficiency of 93% at 28 GHz resonant frequency. The fabricated front view is shown in Fig. 14(a) and *S*-parameters are shown in Fig. 14(b) [87].

To enhance the gain, a 1×4 elliptical patch antenna array was designed on Rogers RT/duroid 5880 substrate ($\epsilon_r = 2.2$, $h = 0.508$ mm, $\tan\delta = 0.0013$) with a size of $6 \times 6\,\text{mm}^2$ and operated at 28 and 45 GHz resonating frequencies. The antenna array achieved a gain of 7.6 dBi and radiation efficiency of 85.6% in the operating frequency band at 28 GHz. SAR for 28 GHz reported was 1.25 W/kg. The fabricated view, *S*-parameters, and radiation patterns are shown in Figs 15(a), 15(b), and 15(c) [88].

For obtaining low side lobe level and bandwidth enhancement, tapering is employed in array antennas. Amplitude tapering can be done by varying the width of the radiating elements. Amplitude tapering function is defined by equations (25) and (26), respectively [89, 90]:

$$w[k] = \cos^2\left[\frac{2\pi}{N}\right]; \quad 0 \le k \le N-1 \tag{25}$$

$$w[1] = \alpha + (1-\alpha)w[k] \tag{26}$$

where α is the pedestal height and $w[1]$ is the new coefficient which is obtained by previous weight $w[k]$.

Amplitude tapering in binomial array is done by varying the effective width of the radiating elements according to equations

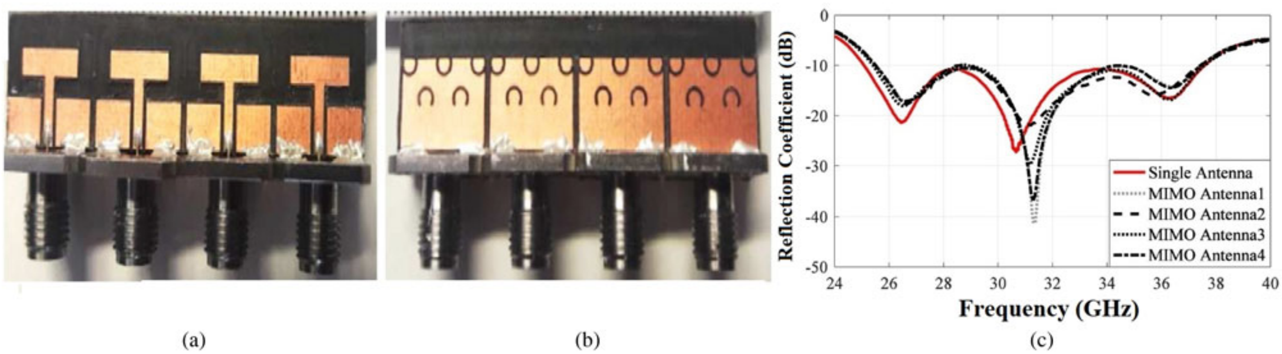

Fig. 25. DGS-based four-element MIMO antenna array: fabricated (a) front view, (b) back view, and (c) *S*-parameters. [104].

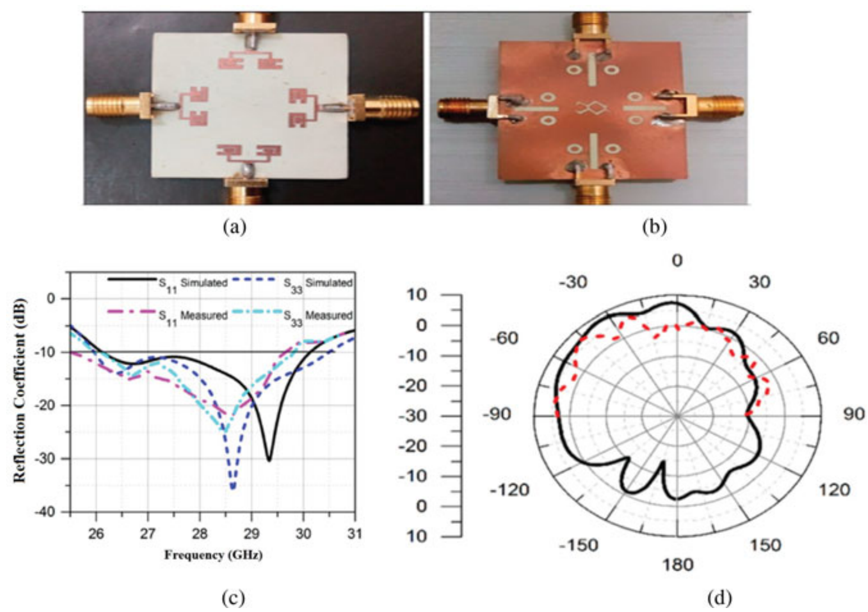

Fig. 26. Four-element MIMO antenna array with multiple DGS: fabricated (a) front view, (b) back view, (c) *S*-parameters, and (d) radiation patterns. [105].

(27) and (28), respectively [91, 92]:

$$B_k = \frac{C_k^{N-1}}{C_{(N-1)/2}^{N-1}} \tag{27}$$

$$C_k^{N-1} = \frac{(N-1)!}{k!(N-1-k)!} \tag{28}$$

where $k = 0, 1, 2, \ldots, N-1$.

A broadband hexagonal antenna array having dimensions of $45 \times 20\,\text{mm}^2$ was designed on Rogers RT/duroid 5880 substrate ($\epsilon_r = 2.2$, $h = 0.254$ mm, $\tan\delta = 0.0009$) in 25.05–34.92 GHz operating band. The geometry of the antenna array utilized two hexagonal wire loops which are concentric and separated by a small gap. The combination of loop and gap gives the flexibility to control the resonant frequency. The single element is backed by a ground loop of the same dimension as that of top wire loops to improve the broadside radiations. A series of vias were used in an inverted U-shape manner. The gain and radiating efficiency achieved were found to be 10.12 dBi and 85% at 28 GHz. The fabricated (front and back) views are shown in Figs 16(a) and 16(b). The gain–efficiency plot is shown in Fig. 16(c) [93].

To increase the gain and efficiency, a single port compact 12 element patch antenna array was designed on Rogers RT/duroid 5880 substrate ($\epsilon_r = 2.2$, $h = 0.79$ mm, $\tan\delta = 0.0009$) with a size of $51.44 \times 18.34\,\text{mm}^2$ in 27.06–28.35 GHz operating band. The four corners of the patches were chopped at an angle of 45° to get minimum return loss. The gain reported was 16.0 dBi with 93.5% radiation efficiency at 28 GHz. The fabricated (front and back) views are shown in Figs 17(a) and 17(b). The *S*-parameters and *E*-field radiation patterns are shown in Figs 17(c) and 17(d) [94].

A 13-circular radiating element grid antenna was designed having dimensions $21.5 \times 23\,\text{mm}^2$ on Rogers RT/duroid 5880 substrate ($\epsilon_r = 2.2$, $h = 0.79$ mm, $\tan\delta = 0.0009$) at 30 GHz resonant frequency. The antenna array achieved a gain of 9 dBi and radiation efficiency of 80% in the operating band 27.5–33.3 GHz. The fabricated view, *S*-parameters, and radiation patterns are shown in Figs 18(a), 18(b), and 18(c) [95].

https://doi.org/10.1017/S1759078722000095 Published online by Cambridge University Press

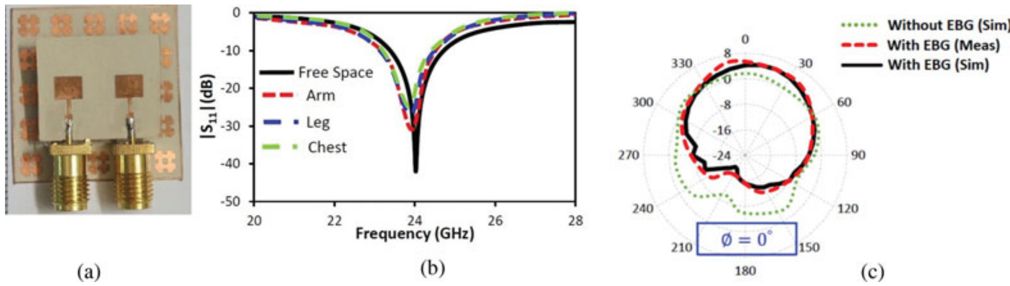

Fig. 27. MIMO antenna with EBG structure: fabricated (a) front view, (b) *S*-parameters, and (c) radiation patterns. [110].

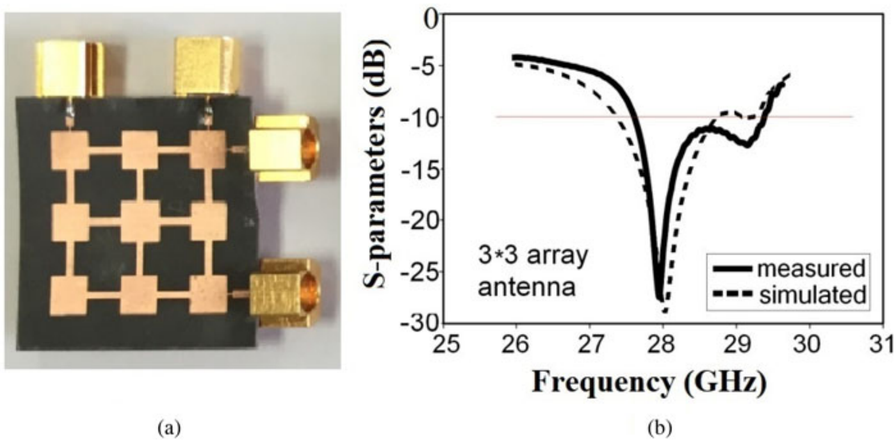

Fig. 28. 3×3 phased antenna array: fabricated (a) front view and (b) *S*-parameters. [113].

For 5G, high gain and compact antennas are highly desirable. A tapered high gain and compact antenna array with series and parallel feeds was designed on Rogers RT/duroid 5880 substrate ($\epsilon_r = 2.2$, $h = 0.79$ mm, $\tan\delta = 0.0009$) with a size of $30 \times 26\,\text{mm}^2$ in 27.70–28.78 GHz operating band. The gain was 17.7 dBi with 93.36% radiating efficiency at 28 GHz resonant frequency. The design steps are shown in Fig. 19 (a). The return loss of all the design steps and *E*-field radiation patterns are shown in Figs 19(b) and 19(c) [96].

In 5G antennas, the bandwidth enhancement could be made by employing feeding techniques such as proximity and aperture coupled because they provide wider bandwidths and prevent undesired radiation as compared to the direct feed structures. A compact size, high gain broadband 6×5 proximity coupled antenna array was designed on two stacked Taconic TLY-5 ($\epsilon_r = 2.2$, $h = 0.51$ mm, $\tan(\delta) = 2.20$). Amplitude tapering was applied by using Dolph–Chebyshev polynomials to the individual patch elements to obtain low sidelobe levels up to -18 dB. However, it produced reflection which was overcome by located slits in the appropriate position. The antenna achieved a gain of around 21 dBi over an operating bandwidth of 27.5–28.5 GHz. The fabricated front and back views are shown in Figs 20(a) and 20(b). The *S*-parameters are shown in Fig. 20 (c) [97].

A Franklin antenna is important for the 5G applications due to its small size, simple structure, high gain, and capability to minimize spurious radiation and surface wave excitation. A multi resonance, compact, and high gain 3×3 Franklin antenna array was designed on a Rogers 5880 substrate ($\epsilon_r = 2.2$, $h = 0.79$ mm, $\tan\delta = 0.0009$) in the operating band of 28 GHz and 37–39 GHz. A Franklin antenna consists of two radiating elements, the first one is the patch and the folded stub. The gains achieved for multiple bands were 13.5 dBi at 29 GHz, 8.33 dBi at 33 GHz, and 9.58 dBi at 38 GHz respectively. The fabricated front view is shown in Fig. 21(a), *S*-parameters and the radiation patterns are shown in Fig. 21(b) and 21(c) [98].

24–40 GHz: MIMO antennas and MIMO antenna arrays

MIMO systems, using an array of antennas at the transmitter and receiver link, provide drastically enhanced data capacity. The ability to achieve this high capacity is greatly determined by the shape, size, and distance between the antennas. There are several studies available in the literature which focus on MIMO antennas and MIMO antenna arrays operating in the mm-wave band for 5G wireless applications. MIMO antennas minimize the effect of multipath propagation by providing a high data rate, increased capacity, and link reliability, which are the main characteristics of 5G. However, the difficulties related to MIMO antenna designing is to design compact antenna elements with reduced mutual coupling and high isolation [99, 100].

A two-element MIMO antenna was designed on a Rogers RT/Duroid 5880 substrate ($\epsilon_r = 2.2$, $h = 0.38$ mm, $\tan\delta = 0.0009$) with a size of $12 \times 24\,\text{mm}^2$ in the operating band of 28.2–30.7 GHz. The ECC value reported was <0.001. The fabricated front view and *S*-parameters are shown in Figs 22(a) and 22(b) [101].

A four-element high gain MIMO antenna was designed and fabricated on a Rogers-5880 substrate ($\epsilon_r = 2.2$, $h = 1.57$ mm, $\tan\delta = 0.0009$) with dimensions of $80 \times 80\,\text{mm}^2$. The antenna gain was 12 dBi with 70% radiating efficiency in the frequency band of 23–40 GHz. The isolation reported was >20 dB and

https://doi.org/10.1017/S1759078722000095 Published online by Cambridge University Press

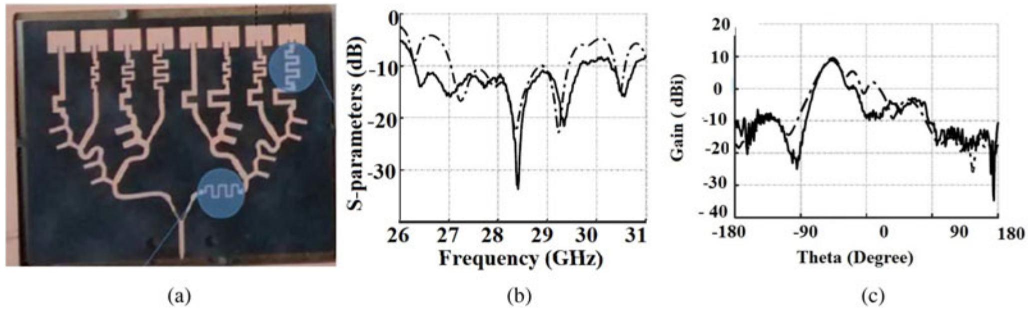

Fig. 29. 1×8 phased antenna array: fabricated (a) front view, (b) *S*-parameters, and (c) radiation patterns. [114].

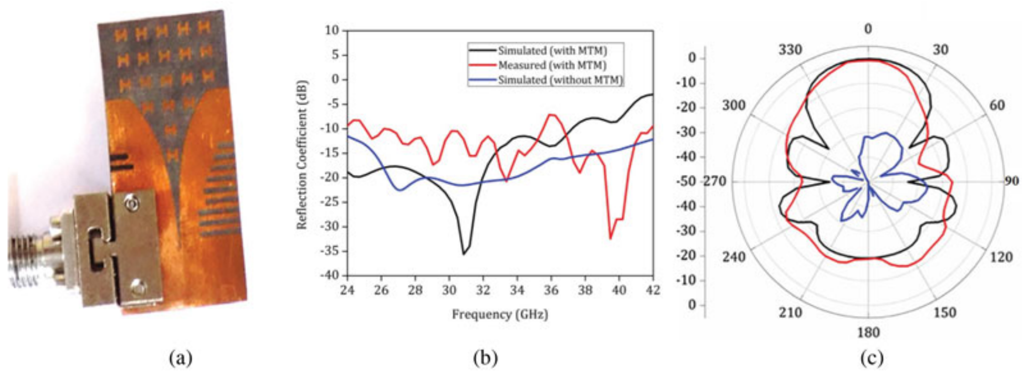

Fig. 30. Metamaterial-based Vivaldi 5G antenna: fabricated (a) front view, (b) *S*-parameters, and (c) radiation patterns. [121].

ECC < 0.0014. The fabricated front view and *S*-parameters are shown in Figs 23(a) and 23(b) [102].

DGS is one of the techniques to suppress the surface wave and improve the performance of an antenna or antenna array. It also helps to reduce the mutual coupling of MIMO elements. An MIMO antenna was designed on a Rogers RT/duroid 5880 substrate ($\epsilon_r = 2.2$, $h = 0.8$ mm, $\tan\delta = 0.0009$) of dimensions 12×25.4 mm^2 in the operating bands of 26.83–33.13 and 34.17–38.13 GHz, respectively. To improve the bandwidth and gain, T-shaped patch was employed in the upper layer of the substrate and the bottom layer utilized the DGS and CSRR. The peak gain measured was 7.2 dBi in the complete operating band. The ECC and DG values were <0.005 and close to 10, respectively. The fabricated (front and back) views are shown in Figs 24(a) and 24(b). The *S*-parameters are shown in Fig. 24(c) [103].

A wide bandwidth four-element MIMO antenna was designed on a Rogers RT/duroid 5880 ($\epsilon_r = 2.9$, $h = 0.254$ mm, $\tan(\delta) = 0.0009$) of dimensions 12×50.8 mm^2 in the operating band 25.1–37.5 GHz. The four T-shaped radiators were designed on top of the substrate and a partial ground loaded with multiple split-ring slots was employed at the bottom. The gain was above 5.0 dBi with 80% radiating efficiency in the complete operating band. The fabricated front view, back view, and *S*-parameters are shown in Figs 25(a), 25(b), and 25(c) [104].

A four-port MIMO antenna array for 5G MIMO applications was designed and fabricated on a Rogers R04350B substrate ($\epsilon_r = 3.66$, $h = 0.79$ mm, $\tan\delta = 0.0037$) having dimensions of 30×35 mm^2. To improve the radiation characteristics and reduce the mutual coupling in the 25.5–29.6 GHz operating band the ground plane defected with the three different slots such as rectangular, circular, and zigzag. The isolation reported between the antennas was 17 dB. The gain and radiating efficiency were 8.3 dBi and 82% respectively with -10 dB impedance bandwidth lies in 25.5–29.6 GHz and ECC < 0.01, and DG > 9.96 were calculated respectively. The fabricated front view, back view, *S*-parameters, and radiation patterns are shown in Figs 26(a), 26(b), 26(c), and 26(d) [105].

EBG structure-based antennas are very popular in mm-wave applications because of their specific band gap characteristics at particular or desired frequency bands. EBG structures can resonate at lower frequencies depending upon the shape and dimension of unit cells, therefore are capable of antenna miniaturization. An EBG consists of periodic or non-periodic arrangement of unit cells which can create high impedance to block the unwanted surface waves for all angles and for all polarization states and field coupling. As a result the gain, efficiency and other parameters of the antennas can be improved. Equations (29)–(32) are generally employed to extract the permittivity and permeability [106–109]:

$$z = \pm\sqrt{\frac{(1+S_{11})^2 - S_{21}^2}{(1-S_{11})^2 - S_{21}^2}} \tag{29}$$

$$e^{j\eta k_0 d} = \frac{S_{21}}{1 - S_{11}((z-1)/(z+1))} \tag{30}$$

$$\epsilon = \frac{\eta}{z} \tag{31}$$

https://doi.org/10.1017/S1759078722000095 Published online by Cambridge University Press

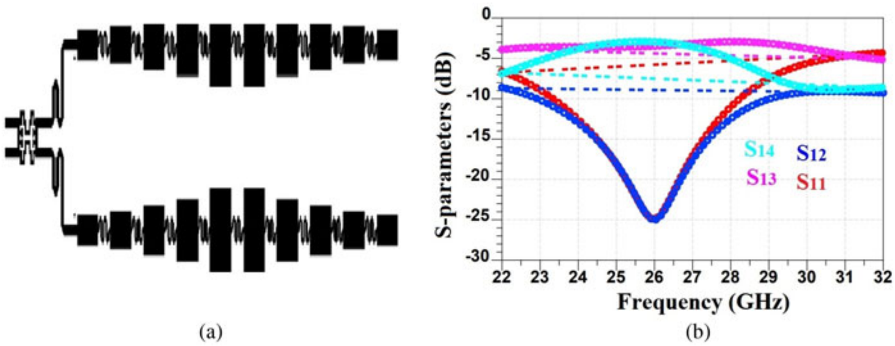

Fig. 31. 2×10 antenna array: schematic (a) front view and (b) *S*-parameters. [124].

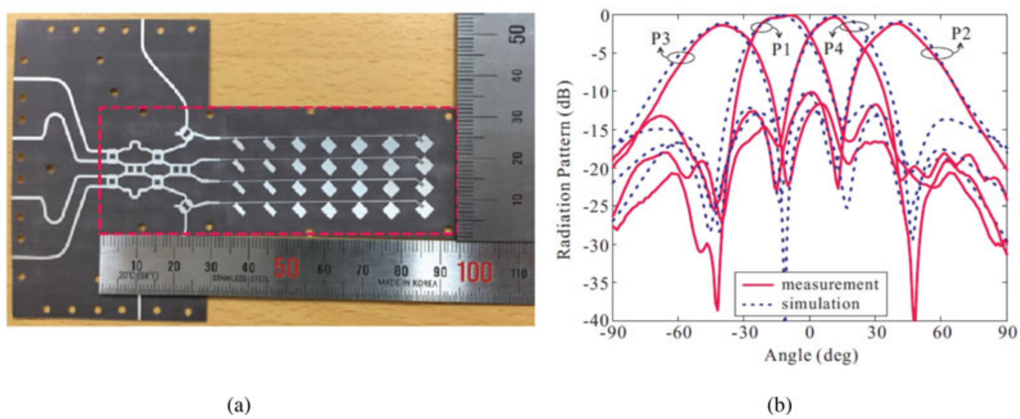

Fig. 32. 5G 4×4 antenna array with Butler matrix: fabricated (a) front view and (b) radiation patterns. [130].

$$\mu = \eta \times z \tag{32}$$

where z is the normalized impedance, k_0 is the wave number, and d is the thickness of the substrate.

In view of mm-wave 5G wearable applications, a two-element MIMO antenna was designed on a flexible Rogers RT/duroid 6002 substrate of dimensions $19.04 \times 15.06\,\text{mm}^2$ ($\epsilon_r = 2.94$, $h = 0.254$ mm, $\tan\delta = 0.0012$). A 5×5 EBG was employed on the back which enhanced the gain by 1.9 dBi and decreased the impact of harmful radiations on the human body. The gain and radiation efficiency achieved were 6.0 dBi and 80.5% at 24 GHz resonant frequency respectively. The fabricated front view, *S*-parameters, and radiation patterns are shown in Figs 27(a), 27(b), and 27(c) [110].

Phased array antenna

A phased array antenna is a combination of antenna elements collected together such that the combined radiation pattern intensifies in the desired direction and diminishes in the undesired direction. Phase antennas reinforced the radiated energy in the desired direction. The gain of the phased array can be calculated by using equation (33), if the correct location of the array element's phase center is unknown:

$$G_{array} = G_1 e^{kd\sin(\theta)+\beta_1} + G_2 e^{kd\sin(\theta)+\beta_2} + \cdots + G_N e^{kd\sin(\theta)+\beta_N} \tag{33}$$

The gain of the phased array, when the accurate location of the array element's phase center is given by equation (34):

$$G_{array} = G_1 e^{j\beta_1} + G_2 e^{j\beta_2} + \cdots + G_N e^{j\beta_N} \tag{34}$$

where G_1, G_2,…, G_N are gains of each antenna elements, k is the wave number, θ is the angle between the array scanning direction and boresight direction, and β_1,…, β_N are the phase shifts in each element's feed [111, 112].

A 3×3 phased antenna array with four feed ports and controlled by four-phase shifters was designed on an RT/duroid 5880 substrate ($\epsilon_r = 2.2$, $h = 0.254$ mm, $\tan\delta = 0.0009$) of dimensions $21 \times 2\,\text{mm}^2$ in the operating band of 27.61–28.43 GHz. The design has the capacity to reduce the number of feed ports and also the phase shifter. The beam steering was obtained by tuning the phase of only one port. The isolation was >29 dB. The gain reported was 14.9 dBi with 73% radiating efficiency for -110° phase at 28 GHz resonant frequency. The fabricated front view and *S*-parameters are shown in Figs 28(a) and 28(b) [113].

To minimize the scan loss and to minimize the sidelobe level, a low cost eight elements rectangular phased array excited by amplitude tapering networks was designed on a Rogers RT/duroid 5880 substrates ($\epsilon_r = 2.2$, $h = 0.254$ mm, $\tan\delta = 0.0009$) with a size of $40 \times 50\,\text{mm}^2$ in the operating band of 27.5–28.65 GHz. The SLL reported was –15.2 dB. The beam steering from $0^\circ-$ to 48° was obtained by varying the dimensions of the meander lines. The gain achieved was 13.6 dBi with a radiation efficiency of 66%. The fabricated front view, *S*-parameters and radiation patterns are shown in Figs 29(a), 29(b), and 29(c) [114].

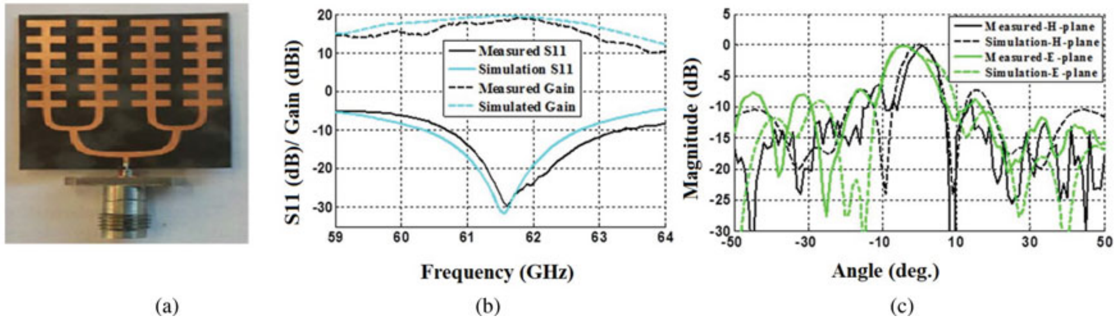

Fig. 33. 4 × 6 antenna array: fabricated (a) front view, (b) *S*-parameters, and (c) radiation patterns. [135].

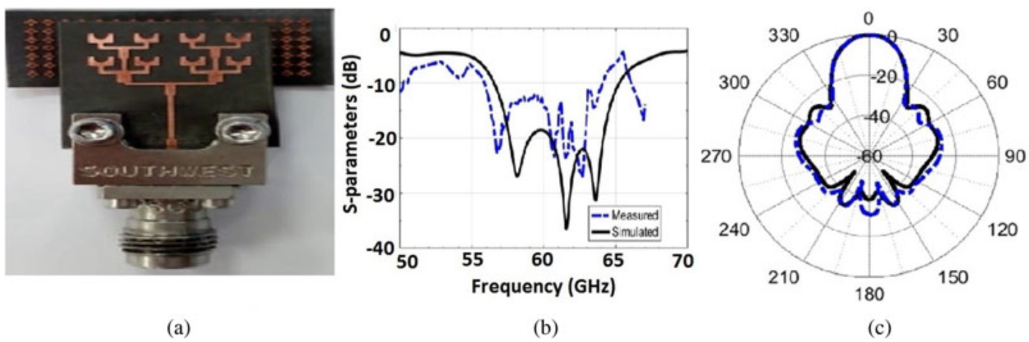

Fig. 34. Eight element antenna array: fabricated (a) front view, (b) *S*-parameters, and (c) radiation patterns. [136].

Beamforming

In the present scenario, every user wants higher data speed and reliable service which can be expected from 5G mobile services. However, as the users and their requirements of the faster data rise rapidly, the base stations will face problems handling such bulk of traffic. For handling such demands beamforming technologies have been adopted. The World Radio-communication Conference (WRC)-15 decided to assign frequency bands for future mobile communications in the mm-wave range such as 24.25–27.5, 27.5–29.5, 37–43.5, 45.5–47, 47.2–48.2, and 66–71 GHz frequency bands. In the USA, the frequency band, n261 28 GHz (27.50–28.350 GHz), n258 24 GHz (25.25–24.45 GHz, and 27.75–25.25 GHz) were announced in 2019 [115, 116].

5G provides enhanced bandwidth in mm-waves frequency up to 500 MHz but as we increase the frequency, the propagation losses and attenuation are very severe. The propagation losses faced by the mm-waves are atmospheric attenuation 0.06–0.2 dB/km in 28–50 GHz frequency range, rain attenuation 6–10 dB/km in 28–60 GHz, diffraction loss 40 dB due to building corner, hail losses of 25 dB at 38 GHz, building penetration losses due to external brick wall and external tinted glass are 28.3 dB and 40.1 dB respectively at 28 GHz, and human body loss is 40 dB at 20 GHz. Therefore, beamforming techniques are seriously required to overcome the propagation loss and boost the signal strength and coverage area [117, 118].

Beamforming is a technique in which BS concentrates energy to the target mobile user and reduces interference to nearby mobile users, thereby improving signal coverage and strength. It is an enabling technique for wireless communications over higher frequency bands, e.g. mm-wave frequency band. The most known beamforming techniques are analog beamforming (ABF), digital beamforming (DBF), and hybrid beamforming (HBF).

It is a well-known fact that beamforming is a crucial element of 5G systems. The distance between the radiating elements (d) and the length of the transmission lines (L_t) are the two factors those decide the final position of the main beam while scanning. The scanning angle can be calculated by using equations (35) and (36), respectively [119, 120]:

$$\theta = \sin^{-1}\left(\frac{L_t}{2D}\right)\left(\frac{\Delta f}{f_c}\right) = \frac{\Delta\phi}{360}\left(\frac{\lambda_0}{D}\right) \tag{35}$$

$$\Delta f = f_c - f_0 \tag{36}$$

where θ is the beam steering direction, f_c indicates the center frequency at which the main beam is located, and $\Delta\phi$ is the phase shift between two connected antenna elements.

The beam direction can also be defined by equation (37):

$$\theta = \sin^{-1}\left(\frac{\lambda - \sqrt{\epsilon l}}{d}\right) \tag{37}$$

A wideband, high gain Vivaldi antenna was designed on a Rogers RT/duroid 5870 substrate ($\epsilon_r = 2.33$, $h = 0.254$ mm, $\tan\delta = 0.0012$) at 28 and 38 GHz resonant frequencies of size $15.5 \times 32\,\text{mm}^2$. The H-shaped metamaterial unit cell was employed in the radiating aperture of the antenna to enhance the aperture efficiency by correcting the phase in the complete operating frequency band. The gain achieved was 12.5 dBi with 78% aperture efficiency at 28 GHz resonant frequency. In addition, a stacked pattern diversity antenna module was also implemented which achieved wide-angle coverage of -60° to $+60^\circ$

https://doi.org/10.1017/S1759078722000095 Published online by Cambridge University Press

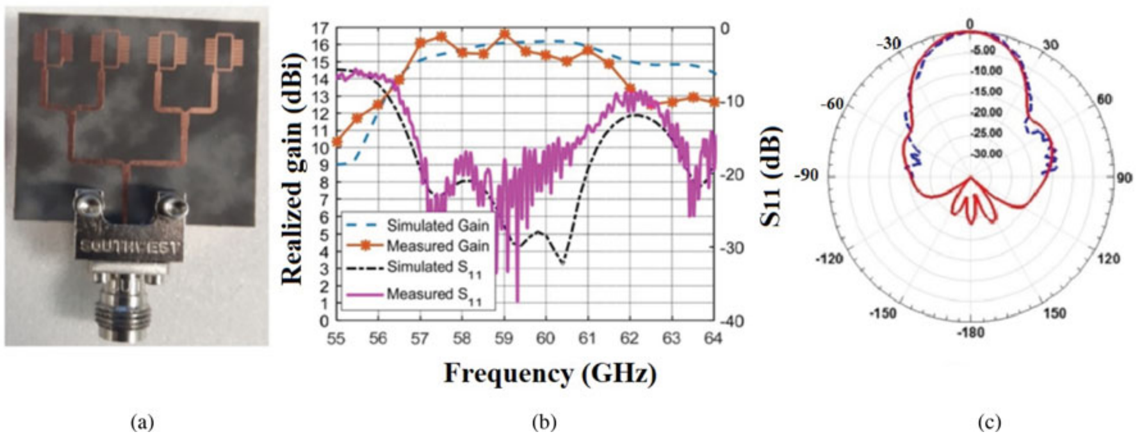

Fig. 35. High gain antenna array: fabricated (a) front view, (b) *S*-parameters, and (c) radiation patterns. [137].

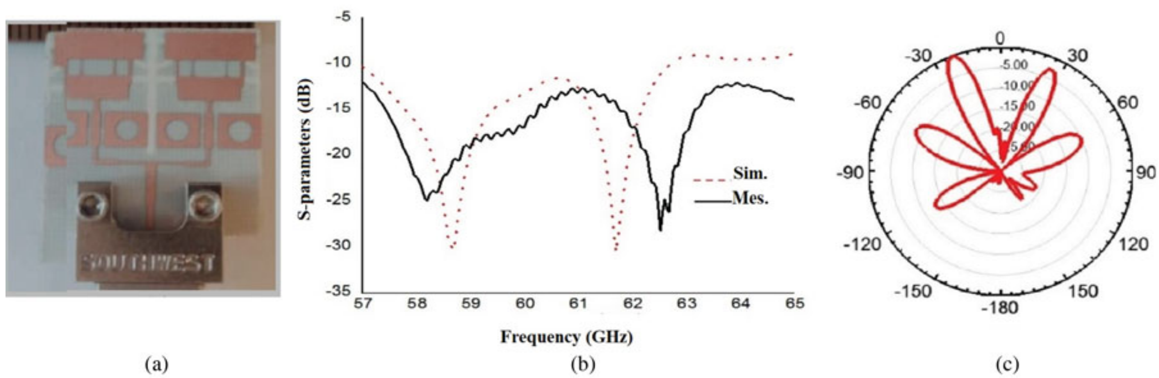

Fig. 36. Monopole T-shaped antenna array: fabricated (a) front view, (b) *S*-parameters, and (c) radiation patterns. [138].

with the beam directed at 0°, +45°, and −45°. The fabricated front view, *S*-parameters, and radiation patterns are shown in Figs 30(a), 30(b), and 30(c) [121].

Switched beam antenna as a smart antenna has been used in 5G antenna system as the implementation of it is simple and requires less cost as compared to phased antenna arrays. It consists of an antenna array and beamforming network such as Butler matrix, and hybrid line coupler. The $n \times n$ Butler matrix is used as a beamforming system and it generates the n-beams, which are linearly spaced phase difference at its output ports. The Butler matrix design is widely used due to its simple design and its ability to form orthogonal narrower beams which are highly directive and therefore the antenna has a low side lobe level [122, 123].

A 2×10 antenna array excited by branch-line hybrid coupler was designed on a Rogers RT/duroid 6002 substrate ($\epsilon_r = 2.9$, $h = 0.254$ mm, $\tan\delta = 0.0037$) of dimensions $79.42 \times 11.53\ \mathrm{mm}^2$ in the operating band of 23.34–28.25 GHz. The gain reported was 14 dBi with a radiating efficiency of 83.82% at 26 GHz resonant frequency. The schematic view of the 2×10 antenna array, and *S*-parameters are shown in Figs 31(a) and 31(b) [124].

The normalized array factors for a 4×4 with a uniform excitation and a 4×8 Butler matrix are given by equations (38) and (39), respectively, [125, 126]:

$$AF_4 = \frac{\sin(2\psi)}{4\sin(\psi/2)} \tag{38}$$

$$\begin{aligned} AF_8 = {} & 1.724\cos\left(\tfrac{\psi}{2}\right) + 1.509\cos\left(\tfrac{3\psi}{2}\right) \\ & + 1.139\cos\left(\tfrac{5\psi}{2}\right) + \cos\left(\tfrac{7\psi}{2}\right) \end{aligned} \tag{39}$$

where $\psi = kd\cos\,\theta + \beta$.

Multibeam antenna arrays play an important role in 5G mm-wave communications. An array with a Butler matrix feeding network can generate multiple beams by feeding all the input ports active synchronously. There are many techniques that can generate fixed and multiple beams such as Blass matrix, Rotman lens, and dielectric lens. The field radiation pattern of the main beam can be modeled as equation (40):

$$F_1(p, q) = \sum_{n=1}^{N_1} C_{n1} F(p, q) \tag{40}$$

where N_1 is the total number of elements in the array, C_{n1} are called the complex beam excitations, (p, q) represent points in space coordinate given by equation (41) [127–129]:

$$\begin{aligned} p &= \sin(\theta)\cos(\phi) \\ q &= \sin(\theta)\sin(\phi) \end{aligned} \tag{41}$$

To obtain four multiple beams with high gains and reduced sidelobe levels a 4×7 microstrip comb-line array excited and

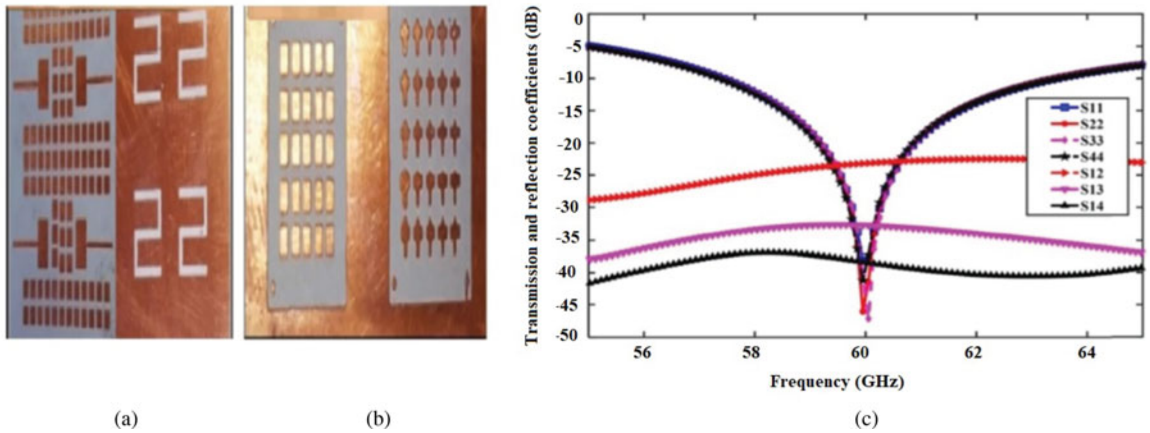

Fig. 37. MIMO antenna with EBG: fabricated (a) front view, (b) EBG view, and (c) *S*-parameters. [139].

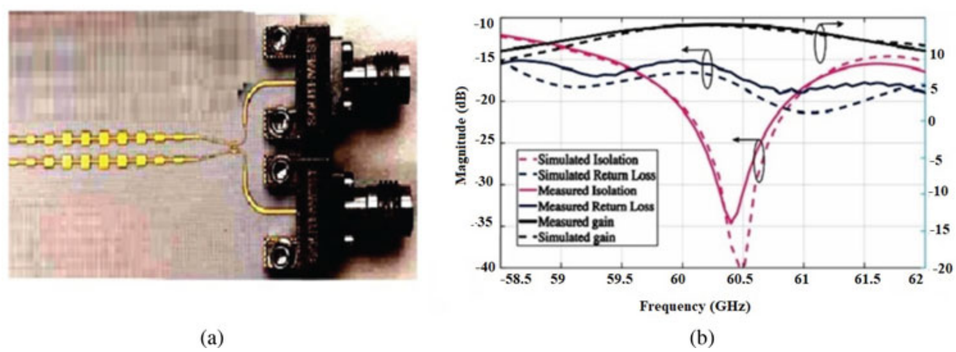

Fig. 38. 1×10 antenna array: fabricated (a) front view and (b) *S*-parameters and gain plot. [142].

integrated with 4×4 Butler matrix (BM) was designed on a Taconic TLY-5 substrate ($\epsilon_r = 2.2$, $h = 0.254$ mm, $\tan\delta = 2.20$) of dimensions $95 \times 32 \times 0.254\,\text{mm}^3$, in the frequency band of 27.525–28.325 GHz. The two attenuators were added to reduce the sidelobe level and also to decrease the coupling between the input ports due to the standing waves from the antenna arrays; the three identical H-slots were employed on the ground plane as decoupling structures. The gain lies in 14.21–17.87 dBi and the four beams were generated by each of the excitation ports pointing toward the directions of $\pm 16.2^0$, $\pm 40.8^0$, $\pm 39.4^0$, and $\pm 12.6°$. The fabricated front view of the butler matrix with antenna array and radiation patterns are shown in Figs 32(a) and 32(b) [130].

5G antenna designs in 60 GHz frequency bands

In this section, various designs of 5G antennas arrays, MIMO antennas, and MIMO antenna arrays, and beamforming antennas in frequency range 57–64 and 64–71 GHz frequency bands are discussed along with their designs and results.

The mm-wave band that lies in the 24–100 GHz frequency band which opens up the new dimensions and challenges for the 5G wireless communication systems. The unlicensed frequency band which lies in 57–61 GHz initiates a large bandwidth possibility for 5G mobile communication that will enhance 5G network capacity which can significantly boost the data rate. To cover the wide bandwidth and to overcome the atmospheric absorption that peaks at 60 GHz at 16 dB/km which requires a high gain antenna, can be accomplished by large antenna arrays. The dimensions of the antenna are given by equations (42) and (43), respectively [131, 132]:

$$W = \frac{2M+1}{\sqrt{(\epsilon_r + 1)/2}} \times \left(\frac{\lambda_0}{2}\right) \tag{42}$$

$$L = \frac{2N+1}{\sqrt{\epsilon_{eff}}} \times \left(\frac{\lambda}{2}\right) - 2\Delta L \tag{43}$$

where M and N are non-negative integers, and λ_0 and λ are free space and operating wavelengths, respectively.

The ΔL is the patch extension due to the fringing field effect. The dimensions of the microstrip feed lines can be measured by employing impedance transformation and the generalized equations are summarized in equations (44) and (45), respectively:

$$Z_{P1} = \frac{9.97\lambda_0}{W} \tag{44}$$

$$W_t = \frac{7.475h}{e^x} - 1.25t \tag{45}$$

https://doi.org/10.1017/S1759078722000095 Published online by Cambridge University Press

Table 3. Comparison of 5G one port 28–40 and 54–71 GHz antennas

Reference	Frequency band/ bands (GHz)	Number of elements	Dimensions (mm^3)	Gain (dBi)	Efficiency (%)	Applications
[87]	27.23–29.89	01	14 × 14 × 1	5.44	93	5G mm-wave applications
[88]	27.4–28.6	04	6 × 6 × 0.508	7.6	85.6	Future 5G Mobile communication Networks
[93]	25.05–34.92	04	45 × 20 × 0.254	10.12	85	Future 5G wireless systems
[94]	27.06–28.35	12	51.44 × 18.34 × 0.79	16.07	93.5	Indoor and outdoor 5G communications
[95]	27.5–33.00	13	21.5 × 23 × 0.79	9.0	80	5G cellular hand held devices
[96]	27.70–28.78	16	30 × 26 × 0.79	17.7	93.36	5G wireless communications
[97]	27.5–28.5	30	96.5 × 102 × 0.51	21.0	–	5G cellular applications
[98]	28.37–39	09	21 × 26 × 0.79	13.5	70	5G wireless networks and satellite communications
[114]	27.5–28.65	08	40 × 50 × 0.254	13.6	66	5G mobile handset and 5G base stations
[135]	61.56	24	27.05 × 31.62 × 0.127	19.26	–	Wireless local area network, Wireless personal area network
[136]	56.5–65.2	08	17.5 × 22 × 0.381	17.0	80	Broadband communications
[137]	60.0	08	5.7 × 4.1 × 0.254	17.5	98	mm-wave applications
[138]	57.2–63.8	08	20.64 × 20 × 0.203	11.6	85	5G mm-wave communications

The x is dependent on the substrate thickness (h) and copper cladding (t) can be defined by equation (46):

$$x = \frac{(Z_c\sqrt{\epsilon_r + 1.41})}{87} \tag{46}$$

The spacing between the patch elements is defined by equation (47):

$$L_s = 2A + 1 \times \left(\frac{\lambda}{2}\right) + 2\Delta L \tag{47}$$

The inter-separation distance between the parallel arms are computed by equation (48):

$$S = 2B + 1 \times \left(\frac{\lambda}{2}\right) \tag{48}$$

where A and B are the non-negative integers [133, 134].

A high gain 4 × 6 antenna array fed with series–parallel transmission lines was designed on a Rogers RT/duroid 5880 substrate ($\epsilon_r = 2.2$, $h = 0.127$ mm, $\tan\delta = 0.0009$) with a size of $27.05 \times 31.62\,mm^2$ for 60 GHz frequency band. In this design patches were excited by the two-stage power dividers and low impedance transmission lines were employed by reverse impedance matching method to achieve low power loss. The gain achieved was 19.26 dBi at 61.56 GHz resonant frequency. The fabricated front view, S-parameters, and radiation patterns are depicted in Figs 33(a), 33(b), and 33(c) [135].

A compact and high-gain antenna array of eight-element was designed on a Rogers 5880 substrate ($\epsilon_r = 2.2$, $\tan\delta = 0.0009$, $h = 0.381$ mm) with a size of $17.5 \times 22\,mm^2$ in the operating frequency band of 56.5–65.2 GHz for mm-wave band applications. The patches were partially circularly slotted and the ground was defected with a circular-shaped slot, respectively to get the proper impedance matching. An EBG reflector consisting of $7 \times 17\,mm^2$ unit cells below the array structure was employed to decrease backward radiation and to improve the front-to-back (F/B) lobe radiation ratio. The gain achieved was 17 dBi with radiating efficiency of 97% at 60 GHz. The fabricated front view, S-parameters and radiation patterns are shown in Figs 34(a), 34(b), and 34(c) [136].

A high gain, mm-wave antenna array was designed on Rogers RT/duroid substrate ($\epsilon_r = 2.2$, $h = 0.254$ mm, $\tan(\delta) = 0.0009$) of dimensions $5.7 \times 4.1\,mm^2$ operating at 60 GHz resonant frequency for mm-wave application. The concept of microstrip line discontinuities was utilized to enhance the performance parameters of the antenna such as gain and radiating efficiency. The left stubs and the right stubs along with square loops were tuned mutually to get proper impedance matching. The antenna gain and radiating efficiency reported were 17.5 dBi and 98% at 60 GHz resonant frequency. The fabricated front view, S-parameters, and radiation patterns are shown in Figs 35(a), 35(b), and 35(c) [137].

A monopole antenna array was designed on a Rogers RO4003 substrate ($\epsilon_r = 3.55$, $h = 0.203$ mm, $\tan(\delta) = 0.00027$) with a size of $20.64 \times 20\,mm^2$ for operating in 57.2–63.8 GHz frequency band. To improve the radiation characteristics, T-shaped slots and stubs were employed in the design. Also to enhance the bandwidth DGS was utilized. The gain of the antenna was 11.6 dBi with 85% radiating efficiency at 60.5 GHz resonant frequency. The antenna covered bandwidth from 57.2 to 63.8 GHz. The fabricated front view, S-parameters, and radiation patterns are shown in Figs 36(a), 36(b), and 36(c) [138].

An MIMO antenna with different EBG structures was designed on a Rogers ULTRALAM substrate ($\epsilon_r = 2.9$, $h = 0.1$ mm, $\tan\delta = 0.0025$) of dimensions $13 \times 14\,mm^2$ for operating in 57–63 GHz frequency band. To decrease the mutual coupling between the antenna elements and to improve the radiation characteristics different EBG structures were employed. The gain and isolation reported were 14.8 dBi and 52.0 dB at 60 GHz resonant frequency,

Table 4. Comparative analysis of 5G 28–40 and 54–71 GHz MIMO antennas

Reference	Frequency band/bands (GHz)	Number of ports	Number of elements	Dimensions (mm^3)	Gain (dBi)	Efficiency (%)	Isolation (dB)	Applications
[101]	27.5–28.365	02	02	12.8 × 26 × 1.6	6.68	80	41.6	5G cellular mobile communication
[102]	23.0–40.0	04	04	80 × 80 × 1.57	12.0	70.0	20	Wideband MIMO applications
[103]	26.5–38.2	02	02	12 × 25.4 × 0.6	6-8	–	–	5G based vehicular communications
[104]	25.1–37.5	04	04	12 × 50.8 × 0.8	5.0	80.0	22	5G MIMO systems and services
[105]	25.5–29.6	04	04	30 × 35 × 0.79	8.3	82.0	17	5G MIMO wireless communications
[110]	24.0	02	02	19.04 × 15.06 × 0.254	7.45	80.5	37	5G MIMO wearable communications
[113]	27.61–28.43	04	09	21 × 21 × 0.254	14.9	73.0	29	Future 5G mm-wave communications
[124]	23.34–28.25	02	20	11 × 79.42 × 0.254	14.0	83.82	25	Future 5G mobile applications
[130]	27.52–28.32	04	16	95 × 321 × 0.254	17.87	–	15	5G wireless systems
[139]	57.0–63.0	04	04	13 × 14 × 0.1	14.8	–	50	MIMO communications
[142]	59.5–61.3	02	20	13 × 30 × 0.2	12.93	–	> 15	Handsets for 5G communication

respectively. The fabricated front view, EBG view, S-parameters, and gain plot are shown in Figs 37(a), 37(b), and 37(c) [139].

The small carrier wavelengths at mm-wave frequencies enable the synthesis of compact antenna arrays, providing beamforming gains that compensate for the increased propagation losses. mm-wave communication is a key technology for future wireless networks. To combat significant path loss and exploit the abundant mm-wave spectrum, effective beamforming is crucial. To overcome the severe link loss, a mm-wave array beamforming technology has been essentially adopted to the 60 GHz Wi-Fi system. The mm-wave beamforming technology enables the directional high gain in an array antenna, where the array antenna pattern can be electronically controlled to the desired direction. The high gain of the array antenna may compensate for the high signal attenuation. Moreover, the electric beam-location control can be utilized to search and find the best antenna pattern even upon the channel variation (e.g. human blockage). Therefore, beamforming technology plays a key role in maintaining the multi-gigabit data transfer link to enable the aforementioned 60 GHz Wi-Fi applications [140, 141].

Switched-beam antenna array plays an important role in hybrid beamforming. A four-layer PCB stack structure was used to design a 2 × 10 antenna array having the capability of generating three beams for a 60 GHz communication system. The 2 × 10 tapered antenna array was designed by employing a 1:0.91:0.74:0.54:0.38 Chebyshev tapering ratio on a Rogers RO4003 substrate ($\epsilon_r = 3.38$, $h = 0.2$ mm, $\tan(\delta) = 0.0027$) for operating in 59.5–61.3 GHz frequency band. All the beams were switched and maximum gain was observed at θ equals 0°, −20°, and 20°. The gain was 12.93 dBi and the mutual coupling reported was >15 dB at 60 GHz resonant frequency. The fabricated front view and S-parameters are shown in Figs 38(a) and 38(b) [142].

The comparison of 5G single port antennas and MIMO antennas for mm-wave frequency band lies in 28–40 and 54–71 GHz on the basis of different frequency bands, number of elements, gain, efficiency, dimensions along with their applications is presented in Tables 3 and 4.

Conclusion

The 5G wireless communication is the demanding technology due to the tremendous growth of mobile data and extensive need for higher data rates, up to 1 Gbps. The use of recent technologies and techniques such as high gain antenna arrays, MIMO, massive MIMO, mm-wave communication, beamforming, etc., have been extensively used in 5G to enhance the data rates and lower the attenuation loss caused by the mm-wave frequency bands. In this paper, different 5G antennas such as single input ports, multiple input ports, single output ports, multiple output ports have been discussed. The different structures of mutual coupling reduction techniques between the antenna elements such as EBG, PBG, and DGS, were studied in paper. The main focus was to review, analyze, and compare different sub-6 GHz (2–8 GHz) antennas and mm-wave antennas (24–40, 57–64, and 64–71 GHz). The mentioned antenna designs in the paper have achieved >6 dBi gain with radiation efficiency around 80%, and isolation achieved was >20 dB. In addition with these designs, mathematical equations, and radiation characteristics have been discussed in detailin the paper.

References

1. **Jun S, Kang Y, Kim J and Kim C** (2020) Ultra-low-latency services in 5G systems. A perspective from 3GPP standards. *ETRI Journal*, **42**, 721–733.
2. **Nahar T and Rawat S** (2021) Survey of various bandwidth enhancement techniques used for 5G antennas. *International Journal of Microwave and Wireless Technologies*, 1–21.
3. **Rappaport TS, Sun S, Mayzus R, Zhao H, Azar Y, Wang K, Wong GN, Schulz JK, Samimi M and Gutierrez F** (2013) Millimeter wave mobile communications for 5G cellular: It will work. *IEEE Access*, **1**, 335–349.
4. **Ghosh A and Ratasuk R** (2011) *Essentials of LTE and LTE-A*. Cambridge University Press, Cambridge.
5. **del Peral-Rosado JA, Raulefs R, Lopez-Salcedo JA and Seco-Granados G** (2018) Survey of cellular mobile radio localization methods: from 1G to 5G. *IEEE Communications Surveys and Tutorials*, **20**, 1124–1148.
6. **Hong W, Jiang ZH, Yu C, Zhou J, Chen P, Yu Z, Zhang H, Yang B, Pang X, Jiang M, Cheng Y, Al-Nuaimi MKT, Zhang Y, Chen J and He S** (2017) Multibeam antenna technologies for 5G wireless communications. *IEEE Transactions on Antennas and Propagation*, **65**(12), 6231–6249.
7. **Osseiran A, Monserrat JF and Marsch P** (2016) *5G Mobile and Wireless Communications Technology*. Cambridge University Press, Cambridge.
8. **Patnaik A and Kartikeyan MV** (2021) Compact dual and triple band antennas for 5G-IOT applications. *International Journal of Microwave and Wireless Technologies*, 1–8.
9. **Marcus MJ** (2019) ITU WRC-19 spectrum policy results. *IEEE Wireless Communications*, **26**(6), 4–5.
10. **Fuentes M, Carcel JL, Dietrich C, Yu L, Garro E, Pauli V, Lazarakis FI, Grondalen O, Bulakci O, Yu J and Mohr W** (2020) 5G new radio evaluation against IMT – 2020 key performance indicators. *IEEE Access*, **8**, 110880–110896.
11. **Gomez-Barquero D, Li W, Fuentes M, Xiong J, Araniti G, Akamine C and Wang J** (2019) 5G for broadband multimedia systems and broadcasting. *IEEE Transactions on Broadcasting*, **65**(2), 351–355.
12. **Andrews JG, Buzzi S, Choi W, Hanly SV, Lozano A, Soong ACK and Zhang JC** (2014) What will 5G be?. *IEEE Journal on Selected Areas in Communications*, **32**(6), 1065–1082.
13. **Doumanis E, Goussetis G, Vuorio J, Hautio K, Amper O, Kuusmik E and Pallonen J** (2021) Tunable filters for agile 5G new radio base transceiver stations. *IEEE Micro Magazine*, **22**(11), 26–37.
14. **Geyikoglu M, Koc Polat H, Kaburcuk F and Cavusoglu B** (2020) SAR analysis of tri-band antennas for a 5G eyewear device. *International Journal of Microwave and Wireless Technologies*, **12**(8), 754–761.
15. **Rodriguez-Cano R, Zhang S, Zhao K and Pedersen GF** (2020) mm-Wave beam-steerable endfire array embedded in a slotted metal-frame LTE antenna. *IEEE Transactions on Antennas and Propagation*, **68**(5), 3685–3694.
16. **Kushwaha RK, Karuppanan P and Malviya LD** (2018) Design and analysis of novel microstrip patch antenna on photonic crystal in THz. *Physica B: Condensed Matter*, **544**, 107–112.
17. **Malviya LD, Panigrahi RK and Kartikeyan MV** (2016) A multi-standard, wide-band 2 × 2 compact MIMO antenna with ground modification techniques. *International Journal of Microwave and Optical Technology*, **11**(4), 259–267.
18. **Pant R, Malviya L and Choudhary V** (2021) Design and analysis of gain enhancement THz microstrip curvature patch PBG antenna with inset feed. In *Mobile Radio Communications and 5G Networks*, Springer, Singapore, 707–715.
19. **Chen JS** (2005) Studies of CPW-fed equilateral triangular-ring slot antennas and triangular-ring slot coupled patch antennas. *IEEE Transactions on Antennas and Propagation*, **53**(7), 2208–2211.
20. **Balanis CA** (2015) *Antenna Theory: Analysis and Design*. Hoboken, NJ: John Wiley & Sons.
21. **Balanis CA** (2011) *Modern Antenna Handbook*. Hoboken, NJ: John Wiley & Sons.
22. **Giauffret L, Laheurte JM and Papiernik A** (1997) Study of various shapes of the coupling slot in CPW-fed microstrip antennas. *IEEE Transactions on Antennas and Propagation*, **45**(4), 642–646.
23. **Gupta P, Malviya LD and Charhate S** (2019) 5G multi-element/port antenna design for wireless applications: a review. *International Journal of Microwave and Wireless Technologies*, **11**(9), 918–938.
24. **Ndip I, Le TH, Schwanitz O and Lang KD** (2018) A comparative analysis of 5G mm-wave antenna arrays on different substrate technologies, 22nd IEEE International Microwave and Radar Conference, Poznan, Poland, 222–225.
25. **Samineni P, Khan T and De A** (2017) Modeling of electromagnetic band gap structures: a review. *International Journal of RF and Microwave Computer-Aided Engineering*, **27**, e21055.
26. **Bait-Suwailam MM, Siddiqui OF and Ramahi OM** (2010) Mutual coupling reduction between microstrip patch antennas using slotted-complementary split-ring resonators. *IEEE Antennas and Wireless Propagation Letters*, **9**, 876–878.
27. **Coulombe M, Koodiani SF and Caloz C** (2010) Compact elongated mushroom (EM)–EBG structure for enhancement of patch antenna array performances. *IEEE Transactions on Antennas and Propagation*, **8**(4), 1076–1086.
28. **Yang F and Rahmat-Samii Y** (2003) Microstrip antennas integrated with electromagnetic band-gap (EBG) structures: a low mutual coupling design for array applications. *IEEE Transactions on Antennas and Propagation*, **51**(10), 2936–2946.
29. **Guha D and Antar YM** (2010) *Microstrip and Printed Antennas: New Trends, Techniques and Applications*. John Wiley & Sons, Hoboken, NJ, USA).
30. **Hussain R** (2021) Shared-aperture slot-based sub-6-GHz and mm-wave IoT antenna for 5G applications. *IEEE Internet of Things Journal*, **8**(13), 10807–10814.
31. **Malik SA, Muzaffar K, Mir AH and Moon AH** (2021) Extremely close integration of dual band sub-6 GHz 4G antenna with unidirectional mm-wave 5G antenna. *Progress in Electromagnetics Research Letters*, **96**, 73–80.
32. **Han ZJ, Song W and Sheng XQ** (2017) Gain enhancement and RCS reduction for patch antenna by using polarization-dependent EBG surface. *IEEE Antennas and Wireless Propagation Letters*, **16**, 1631–1634.
33. **Haraz OM, Elboushi A, Alshebeili SA and Sebak AR** (2014) Dense dielectric patch array antenna with improved radiation characteristics using EBG ground structure and dielectric superstrate for future 5G cellular networks. *IEEE Access*, **2**, 909–913.
34. **Jiang H, Si LM, Hu W and Lv XA** (2019) Symmetrical dual-beam bow-tie antenna with gain enhancement using metamaterial for 5G MIMO applications. *IEEE Photonics Journal*, **11**(1), 1–9.
35. **Nguyen N and Vu V** (2019) Gain enhancement for MIMO antenna using metamaterial structure. *International Journal of Microwave and Wireless Technologies*, **11**(8), 851–862.
36. **Gonzalez SRM and Marquez RTR** (2019) Microstrip antenna design for 3.1–4.2 GHz frequency band applied to 5G mobile devices. *European Journal of Engineering and Technology Research*, **4**(10), 111–115.
37. **Arya AK, Kim SJ and Kim S** (2020) A dual-band antenna for LTE-R and 5G lower frequency operations. *Progress in Electromagnetics Research Letters*, **88**, 113–119.
38. **Azim R, Meaze A, Affandi A, Alam M, Aktar R, Mia M and Islam M** (2021) A multi-slotted antenna for LTE/5G sub-6 GHz wireless communication applications. *International Journal of Microwave and Wireless Technologies*, **13**(5), 486–496.
39. **An W, Li Y, Fu H, Ma J, Chen W and Feng B** (2018) Low-profile and wideband microstrip antenna with stable gain for 5G wireless applications. *IEEE Antennas and Wireless Propagation Letters*, **7**(4), 621–624.
40. **Singh H, Sohi B and Gupta A** (2020) Designing and performance evaluation of metamaterial inspired antenna for 4G and 5G applications. *International Journal of Electronics*, **108**, 1–23.
41. **Ishteyaq I, Shah Masoodi I and Muzaffar K** (2021) A compact double-band planar printed slot antenna for sub-6 GHz 5G wireless applications. *International Journal of Microwave and Wireless Technologies*, **13**(5), 469–477.

42. **Song R, Huang GL, Liu C, Zhang N, Zhang J, Liu C, Wu ZP and He D** (2019) High-conductive graphene film based antenna array for 5G mobile communications. *International Journal of RF and Microwave Computer-Aided Engineering*, **29**, e21692.
43. **Bhatia SS and Sivia JS** (2018) Analysis and design of circular fractal antenna array for multiband applications. *International Journal of Information Technology*, 1–11.
44. **Tran HH and Park HC** (2020) Gain and bandwidth enhancements of sequential fed circularly polarized patch antenna array using multiple parasitic elements. *International Journal of RF and Microwave Computer-Aided Engineering*, **30**(9), e22319.
45. **Malviya LD, Panigrahi R and Kartikeyan MV** (2017) MIMO antennas with diversity and mutual coupling reduction techniques: a review. *International Journal of Microwave and Wireless Technologies*, **9**(8), 1763–1780.
46. **Khan MU and Sharawi MS** (2015) A dual-band micro-strip annular slot based MIMO antenna system. *Microwave and Optical Technology Letters*, **57**(2), 360–364.
47. **Malviya LD, Panigrahi RK and Kartikeyan MV** (2016) A 2 × 2 dual-band MIMO antenna with polarization diversity for wireless applications. *Progress in Electromagnetics Research C*, **61**, 91–103.
48. **Malik J, Patnaik A and Kartikeyan MV** (2015) Novel printed MIMO antenna with pattern and polarization diversity. *IEEE Antennas and Wireless Propagation Letters*, **14**, 739–742.
49. **Molisch AF, Win MZ, Choi YS and Winters JH** (2005) Capacity of MIMO systems with antenna selection. *IEEE Transactions on Wireless Communications*, **4**(4), 1759–1772.
50. **Arnold BT and Jensen MA** (2019) The effect of antenna mutual coupling on MIMO radar system performance. *IEEE Transactions on Antennas and Propagation*, **67**(3), 1410–1416.
51. **Malviya LD, Panigrahi RK and Kartikeyan MV** (2017) A low profile MIMO antenna with polarization diversity for 1800/1900 applications. *Microwave and Optical Technology Letters*, **59**, 533–538.
52. **Malviya LD, Malik J, Panigrahi RK and Kartikeyan MV** (2015) Design of a compact MIMO antenna with polarization diversity technique for wireless communication, In *IEEE International Conference on Microwave Optical and Communication Engineering*, Bhubaneswar, India, 21–24.
53. **Malviya LD, Parmar A, Solanki D, Gupta P and Malviya P** (2020) Highly isolated inset-feed 28 GHz MIMO-antenna array for 5G wireless application. *Procedia Computer Science*, **171**, 1286–1292.
54. **Malviya LD, Panigrahi RK and Kartikeyan MV** (2018) Multi-standard, multi-band planar multiple input multiple output antenna with diversity effects for wireless applications. *International Journal of RF and Microwave Computer-Aided Engineering*, **29**, 1–8.
55. **Malviya LD, Panigrahi RK and Kartikeyan MV** (2018) Offset planar MIMO antenna for omnidirectional radiation patterns. *International Journal of RF and Microwave Computer-Aided Engineering*, **28**, 1–9.
56. **Hassan AT and Sharawi MS** (2016) Four element half circle shape printed MIMO antenna. *Microwave and Optical Technology Letters*, **58**, 2990–2992.
57. **Chouhan S, Panda DK, Gupta M and Singhal S** (2018) Multiport MIMO antennas with mutual coupling reduction techniques for modern wireless transreceive operations: a review. *International Journal of RF and Microwave Computer-Aided Engineering*, **58**, e21189.
58. **Malviya LD, Panigrahi RK and Kartikeyan MV** (2018) Four element planar MIMO antenna design for long-term evolution operation. *IETE Journal of Research*, **64**(3), 367–373.
59. **Malviya LD, Panigrahi RK and Kartikeyan MV** (2020) *MIMO Antennas for Wireless Communication: Theory and Design*. Boca Raton, FL: CRC Press.
60. **Kildal P and Rosengren K** (2004) Correlation and capacity of MIMO systems and mutual coupling, radiation efficiency, and diversity gain of their antennas: simulations and measurements in a reverberation chamber. *IEEE Communications Magazine*, **42**(12), 104–112.
61. **Glazunov AA, Molisch AF and Tufvesson F** (2009) Mean effective gain of antennas in a wireless channel. *IET Microwaves, Antennas and Propagation*, **3**, 214–227.
62. **Ando A, Taga T, Kondo A, Kagoshima K and Kubota S** (2008) Mean effective gain of mobile antennas in line-of-sight street microcells with low base station antennas. *IEEE Transactions on Antennas and Propagation*, **56**(11), 3552–3565.
63. **Chae SH, Oh SK and Park SO** (2007) Analysis of mutual coupling, correlations, and TARC in WiBro MIMO array antenna. *IEEE Antennas and Wireless Propagation Letters*, **6**, 122–125.
64. **Fritz-Andrade E, Jardon-Aguilar H and Tirado-Mendez JA** (2020) The correct application of total active reflection coefficient to evaluate MIMO antenna systems and its generalization to *N* ports. *International Journal of RF and Microwave Computer-Aided Engineering*, **30**.
65. **Arya AK, Kartikeyan MV and Patnaik A** (2010) Defected ground structure, a review. *Frequenz*, **64**(5-6), 79–84.
66. **Exposito-Dominguez G, Fernandez-Gonzalez JM, Padilla P and Sierra-Castaner M** (2012) Mutual coupling reduction using EBG in steering antennas. *IEEE Antennas and Wireless Propagation Letters*, **11**, 1265–1268.
67. **Reddy BRS and Vakula D** (2017) Compact dual-band truncated patch antenna with fractal defected ground structure for wireless applications. *International Journal of Microwave and Wireless Technologies*, **9**(1), 163–170.
68. **Yang F and Samii YR** (2009) *Electromagnetic Band Gap Structures in Antenna Engineering*. Cambridge University Press, Cambridge.
69. **Mandal MK and Sanyal S** (2006) A novel defected ground structure for planar circuits. *IEEE Microwave and Wireless Components Letters*, **16**(2), 93–95.
70. **Kandwal A, Sharma R and Khah SK** (2013) Bandwidth enhancement using Z-shaped defective ground structure for a microstrip antenna. *Microwave and Optical Technology Letters*, **55**(10), 2251–2254.
71. **Sokunbi O Attia H** (2019) Highly reduced mutual coupling between wideband patch antenna array using multiresonance EBG structure and defective ground surface. *Microwave and Optical Technology Letters*, 1–10.
72. **2020)** Compact sub-6 GHz 5G-multiple-input-multiple-output antenna system with enhanced isolation. *International Journal of RF and Microwave Computer-Aided Engineering*, **30**(8), e22246.
73. **2020)** A compact pattern diversity MIMO antenna with enhanced bandwidth and high-isolation characteristics for WLAN/5G/WiFi applications. *Microwave and Optical Technology Letters*, **62**(6), 2353–2364.
74. **Ojo R, Jamlos MF, Soh PJ, Jamlos MA, Bahari N, Lee YS, Al-Bawri SS, Abdul Karim MS and Khairi KA** (2020) A triangular MIMO array antenna with a double negative metamaterial superstrate to enhance bandwidth and gain. *International Journal of RF and Microwave Computer-Aided Engineering*, **30**(8), e22320.
75. **Ancans G, Bobrovs V, Ancans A and Kalibatiene D** (2017) Spectrum considerations for 5G mobile communication systems. *Procedia Computer Science*, **104**, 509–516.
76. **Hassan WA, Jo HS and Tharek AR** (2015) The feasibility of coexistence between 5G and existing services in the IMT-2020 candidate bands in Malaysia. *IEEE Access*, **5**, 14867–14888.
77. **Yost S, What-does-every-engineer-need-to-know-about-5G. IEEE Spectrum, 1–2.**
78. **Wang T, Li G, Ding J, Miao Q, Li J and Wang Y** (2015) 5G spectrum: is China ready?. *IEEE Communications Magazine*, **53**(7), 58–65.
79. **IMT Vision–Framework and overall objectives of the future development of IMT for 2020 and beyond**. Recommendation ITU-R M. 2083-0, 2015.
80. **Technical feasibility of IMT in bands above 6 GHz**. Report ITU-R M. 2376-0, 2015.
81. **Seker C, Guneser MT and Arslan H** (2020) Millimeter-wave propagation modeling and characterization at 32 GHz in indoor office for 5G networks. *International Journal of RF and Microwave Computer-Aided Engineering*, **30**(12), e22455.
82. **Ioannides P and Balanis CA** (2005) Uniform circular and rectangular arrays for adaptive beamforming applications. *IEEE Antennas and Wireless Propagation Letters*, **4**, 351–354.
83. **Karmakar A** (2021) Fractal antennas and arrays: a review and recent developments. *International Journal of Microwave and Wireless Technologies*, **13**(2), 173–197.
84. **Yadav R, Parmar A, Malviya LD and Nitnaware D** (2021) 28 GHz inset feed circular shaped compact patch antenna array for 5G wireless

communication. In *10th IEEE, International Conference on Communication Systems and Network Technologies*, Bhopal, India, 1-4.
85. **Pant M, Malviya LD and Choudhary V** (2020) Gain and bandwidth enhancement of 28 GHz tapered feed antenna array. In *2020 11th IEEE, International Conference on Computing, Communication and Networking Technologies*, IIT Kharagpur, India, 1-4.
86. **Pant M, Malviya LD and Choudhary V** (2021) A 28 GHz corporate series-fed taper antenna array for fifth-generation wireless communication, In *Mobile Radio Communications and 5G Networks*, Springer, Singapore, 697–705.
87. **Rahman A, Ng M Y, Ahmed AU, Alam T, Singh MJ and Islam MT** (2016) A compact 5G antenna printed on manganese zinc ferrite substrate material. *IEICE Electronics Express*, **13**(11), 1–5.
88. **Khattak MI, Sohail A, Khan U, Barki Z and Witjaksono G** (2019) Elliptical slot circular patch antenna array with dual band behaviour for future 5G mobile communication networks. *Progress in Electromagnetics Research C*, **89**, 133–147.
89. **Yuan T, Yuan N and Li LW** (2008) A novel series-fed taper antenna array design. *IEEE Antennas and Wireless Propagation Letters*, **7**, 362–365.
90. **Singh B, Sarwade N and Ray KP** (2017) Compact series fed tapered antenna array using unequal rectangular microstrip antenna elements. *Microwave and Optical Technology Letters*, **59**(8), 1856–1861.
91. **Chopra R and Kumar G** (2019) Series-fed binomial microstrip arrays for extremely low sidelobe level. *IEEE Transactions on Antennas and Propagation*, **67**(6), 4275–4279.
92. **Jian R, Chen Y, Chen T and Li Z** (2019) Efficient design of compact millimeter wave microstrip linear array with bandwidth enhancement and sidelobe reduction. *International Journal of RF and Microwave Computer-Aided Engineering*, **29**(10), 1–11.
93. **Ullah H and Tahir FA** (2019) A broadband wire hexagon antenna array for future 5G communications in 28 GHz band. *Microwave and Optical Technology Letters*, **61**(13), 696–701.
94. **Malviya LD and Gupta P** (2021) Millimeter wave high-gain antenna array for wireless applications. *IETE Journal of Research*, 1–10.
95. **Jilani SF, Abassi QH and Alomainy A** (2020) Millimetre-Wave MIMO array of a compact grid antenna for 5G wireless networks and beyond. In *IEEE International Conference on UK-China Emerging Technologies*, Glasgow, UK.
96. **Pant M, Malviya L and Choudhary V** (2022) Performance improvement of 28 GHz antenna array for fifth-generation wireless communication system. In *Recent Trends in Electronics and Communication*, Vol. 777, Springer, Singapore, 371–380.
97. **Diawuo HA and Jung YB** (2018) Broadband proximity-coupled microstrip planar antenna array for 5G cellular applications. *IEEE Antennas and Wireless Propagation Letters*, **17**(7), 1286–1290.
98. **Jilani SF and Alomainy A** (2017) A multiband millimeter-wave 2-D array based on enhanced Franklin antenna for 5G wireless systems. *IEEE Antennas and Wireless Propagation Letters*, **16**, 2983–2986.
99. **Yadav R and Malviya LD** (2020) UWB antenna and MIMO antennas with bandwidth, band-notched, and isolation properties for high-speed data rate wireless communication: a review. *International Journal of RF and Microwave Computer-Aided Engineering*, **30**(2), e22033.
100. **Malviya LD, Gupta P, Parmar A, Solanki D and Malviya P** (2019) MIMO antenna design with low ECC for mm-wave. In *IEEE Indian Conference on Antennas and Propagation*, Ahmedabad, India, 1–5.
101. **Hasan MN and Seo M** (2018) Compact Omnidirectional 28 GHz 2 × 2 MIMO Antenna Array for 5G Communications. In *International Symposium on Antennas and Propagation*, Busan, South Korea, 1-2.
102. **Sehrai DA, Abdullah M, Altaf A, Kiani SH, Muhammad F, Tufail M and Rahman S** (2020) A novel high gain wideband MIMO antenna for 5G millimeter wave applications. *Electronics*, **9**(6), 1031.
103. **Venkateswara Rao M, Madhav BT, Krishna J, Usha Devi Y, Anilkumar T and Prudhvi Nadh B** (2020) CSRR-loaded T-shaped MIMO antenna for 5G cellular networks and vehicular communications. *International Journal of RF and Microwave Computer-Aided Engineering*, **29**(8), e21799.
104. **Jilani SF and Alomainy A** (2018) Millimetre-wave T-shaped MIMO antenna with defected ground structures for 5G cellular networks. *IET Microwaves, Antennas and Propagation*, **12**(5), 672–677.
105. **Khalid M, Iffat Naqvi S, Hussain N, Rahman M, Mirjavadi SS, Khan MJ and Amin Y** (2020) 4-Port MIMO antenna with defected ground structure for 5G millimeter wave applications. *Electronics*, **9**(1), 71.
106. **Peddakrishna S, Khan T and De A** (2017) Electromagnetic band-gap structured printed antennas: a feature-oriented survey. *International Journal of RF and Microwave Computer-Aided Engineering*, **27**(7).
107. **Madhav BT, Usha Devi Y and Anilkumar T** (2019) Defected ground structured compact MIMO antenna with low mutual coupling for automotive communications. *Microwave and Optical Technology Letters*, **61** (3), 794–800.
108. **Hussain R, Alreshaid AT, Podilchak SK and Sharawi MS** (2017) Compact 4G MIMO antenna integrated with a 5G array for current and future mobile handsets. *IET Microwaves, Antennas and Propagation*, **11**(2), 271–279.
109. **Yang F and Rahmat-Samii Y** (2009) *Electromagnetic Band Gap Structures in Antenna Engineering.*. Cambridge Univ. Press, Cambridge.
110. **Iqbal A, Basir A, Smida A, Mallat NK, Elfergani I, Rodriguez J and Kim S** (2019) Electromagnetic bandgap backed millimeter-wave MIMO antenna for wearable applications. *IEEE Access*, **7**, 111135–111144.
111. **Syrytsin I, Zhang S, Pedersen GF and Morris AS** (2018) Compact quad-mode planar phased array with wideband for 5G mobile terminals. *IEEE Transactions on Antennas and Propagation*, **66**(9), 4648–4657.
112. **Yu LC and Kamarudin MR** (2016) Investigation of patch phase array antenna orientation at 28 GHz for 5G applications. *Procedia Computer Science*, **86**, 47–50.
113. **Khalily M, Tafazolli R, Rahman TA and Kamarudin MR** (2015) Design of phased arrays of series-fed patch antennas with reduced number of the controllers for 28-GHz mm-wave applications. *IEEE Antennas and Wireless Propagation Letters*, **15**, 1305–1308.
114. **Hill TA and Kelly JR** (2019) 28 GHz Taylor feed network for sidelobe level reduction in 5G phased array antennas. *Microwave and Optical Technology Letters*, **61**(1), 37–43.
115. **Rao LD, Pant M, Malviya L, Parmar A and Charhate SV** (2020) 5G beamforming techniques for the coverage of intended directions in modern wireless communication: in-depth review. *International Journal of Microwave and Wireless Technologies*, **13**(10), 1–24.
116. **Uchendu I and Kelly JR** (2016) Survey of beam steering techniques available for millimeter wave applications. *Progress in Electromagnetics Research B*, **68**, 35–54.
117. **Roh W, Seol JY, Park J, Lee B, Lee J, Kim Y, and Aryanfar F** (2014) Millimeter-wave beamforming as an enabling technology for 5G cellular communications: theoretical feasibility and prototype results. *IEEE Communications Magazine*, **52**(2), 106–113.
118. **Wang H, Zhang Z, Li Y and Iskander MF** (2015) A switched beam antenna with shaped radiation pattern and interleaving array architecture. *IEEE Transactions on Antennas and Propagation*, **63**(7), 2914–2921.
119. **Gholam F, Vía J and Santamaria I** (2011) Beamforming design for simplified analog antenna combining architectures. *IEEE Transactions on Vehicular Technology*, **60**(5), 2373–2378.
120. **Babale SA, Rahim SKA, Barro OA, Himdi M and Khalily M** (2018) Single layered 4 × 4 Butler matrix without phase-shifters and crossovers. *IEEE Access*, **6**, 77289–77298.
121. **Muzaffar K, Magray MI, Karthikeya GS and Koul SK** (2020) Wideband high aperture efficiency antennas with beam switching for mm-wave 5G base stations. *International Journal of RF and Microwave Computer-Aided Engineering*, **30**(8), 1–10.
122. **Li WR, Chu CY, Lin KH and Chang SF** (2004) Switched-beam antenna based on modified Butler matrix with low sidelobe level. *Electronics Letters*, **40**(5), 290–292.
123. **Rao SK** (1999) Design and analysis of multiple-beam reflector antennas. *IEEE Antennas and Propagation Magazine*, **41**(4), 53–59.
124. **Moubadir M, Mchbal A, Touhami NA and Aghoutane M** (2019) A switched beamforming network for 5G modern wireless communications applications. *Procedia Manufacturing*, **32**, 753–761.
125. **Zhang YS and Hong W** (2012) A millimeter-wave gain enhanced multibeam antenna based on a coplanar cylindrical dielectric lens. *IEEE Transactions on Antennas and Propagation*, **60**(7), 3485–3488.

126. **Prasad S, Meenakshi M, Adhithiya N, Rao PH, Krishna Ganti R and Bhaumik S** (2021) mm-wave multibeam phased array antenna for 5G applications. *Journal of Electromagnetic Waves and Applications*, **1**, 1–13.
127. **Guenad B, Meriah SM and Bendimerad FT** (2007) Multibeam antennas array pattern synthesis using a variational method. *Radioengineering-Prague*, **16**(2), 28.
128. **Luh H** (1976) On the radiation pattern of a multibeam antenna. *IEEE Transactions on Antennas and Propagation*, **24**(1), 101–102.
129. **Ershadi SE, Keshtkar A, Bayat A, Abdelrahman AH and Xin H** (2018) Rotman lens design and optimization for 5G applications. *International Journal of Microwave and Wireless Technologies*, **10**(9), 1048–1057.
130. **Trinh-Van S, Lee JM, Yang Y, Lee KY and Hwang KC** (2019) A sidelobe-reduced, four-beam array antenna fed by a modified 4×4 Butler matrix for 5G applications. *IEEE Transactions on Antennas and Propagation*, **67**(7), 4528–4536.
131. **Zhang J, Ge X, Li Q, Guizani M and Zhang Y** (2016) 5G millimeter-wave antenna array: design and challenges. *IEEE Wireless Communications*, **24**(2), 106–112.
132. **Issa K, Fathallah H, Ashraf MA, Vettikalladi H and Alshebeili S** (2019) Broadband high-gain antenna for millimetre-wave 60-GHz band. *Electronics*, **8**(11), 1246.
133. **Jose MC, Radha S, Sreeja BS, Alsath MGN and Kumar P** (2021) Compact dual-band millimeter-wave antenna for 5G WLAN. *International Journal of Microwave and Wireless Technologies*, **1**, 1–8.
134. **Rabbani MS and Ghafouri-Shiraz H** (2017) Ultra-wide patch antenna array design at 60 GHz band for remote vital sign monitoring with Doppler radar principle. *Journal of Infrared, Millimeter, and Terahertz Waves*, **38**(5), 548–566.
135. **Rabbani MS and Ghafouri-Shiraz H** (2017) High gain microstrip antenna array for 60 GHz band point to point WLAN/WPAN communications. *Microwave and Optical Technology Letters*, **59**(3), 511–514.
136. **Ghattas ASW, Saad AAR and Khaled EEM** (2020) Compact patch antenna array for 60 GHz millimeter-wave broadband applications. *Wireless Personal Communications*, **114**, 2821–2839.
137. **Al-Alem Y and Kishk AA** (2018) Efficient millimeter-wave antenna based on the exploitation of microstrip line discontinuity radiation. *IEEE Transactions on Antennas and Propagation*, **66**(6), 2844–2852.
138. **Mneesy TS, Hamad RK, Zaki AI and Ali WA** (2020) A novel high gain monopole antenna array for 60 GHz millimeter-wave communications. *Applied Sciences*, **10**(13), 4546.
139. **Ullah S, Yeo WH, Kim H and Yoo H** (2020) Development of 60-GHz millimeter wave, electromagnetic bandgap ground planes for multiple-input multiple-output antenna applications. *Science Reports*, **10**(1), 1–12.
140. **Horwath BD and Abhari R** (2019) Design and evaluation of a vertically integrated passive two-dimensional beam switching antenna array at 60 GHz. *International Journal of RF and Microwave Computer-Aided Engineering*, **29**(11), e21930.
141. **Aziz I, Dahlback R, Ojefors E, Sjogren K, Rydberg A and Dancila D** (2019) 60 GHz compact broadband antenna arrays with wide-angle beam steering. *The Journal of Engineering*, **2019**(8), 5407–5414.
142. **Liu Y, Bshara O, Tekin I, Israel C, Hoorfar A, Taskin B and Dandekar KR** (2019) Design and fabrication of two-port three-beam switched beam antenna array for 60 GHz communication. *IET Microwaves, Antennas and Propagation*, **13**(9), 1438–1442.

Mohit Pant received his M.E. degree in Digital Communication from the Institute of Engineering & Technology, DAVV, Indore, India in 2012 and his B.E. degree in Electronics and Communication from the Laxmi Narayan College of Technology, Bhopal (M.P.), India in 2004. Currently, he is working as an Associate Professor in the Mahakal Institute of Technology, Ujjain (M.P.), India and pursuing his Ph.D. degree from Shri G. S. Institute of Technology and Science, Indore, India. His current research interest includes millimeter-wave antennas, 5G antenna arrays for wireless applications, and multiple-input–multiple-output (MIMO) antennas for high data rate communications for 5G. He is a member of the IEEE. He holds a patent on ultra-wide-band (UWB) antenna design.

Dr. Leeladhar Malviya received his Ph.D. from IIT Roorkee, India in 2017. He received his M.E. in Electronics and Telecommunication from Shri G. S. Institute of Technology and Science, Indore (M.P.), India, in 2008, and his B.E. in Electronics and Communication from the Government Engineering College, Ujjain (M.P.), India, in 1998. Since 2001, he has been with Shri G. S. Institute of Technology and Science, Indore (M.P.), India, and serving as an Associate Professor. His current research interests include compact multiple-input-multiple-output (MIMO) antennas for high data rate communications for 4G, 5G, and THz planar microstrip antennas, fractal antennas, and metamaterial antennas for communication. He is a Senior Member of IEEE, Fellow Institution of Electronics and Telecommunications Engineers (F-IETE, India), Institution of Engineers (IE, India), and Indian Society for Technical Education (ISTE). He is the reviewer of Elsevier, IEEE, IET, IETE-JR, IJCS, Engineering reports, and PIER journals. He has published a number of book chapters in Springer Singapore publication. He holds a patent on ultra-wide-band (UWB) antenna design. He is also the author of a book, "MIMO Antennas for Wireless Communication: Theory and Design" (CRC Press, 2020, Taylor and Francis).